Inertial MEMS Sensors

by

Majed S. Alghamdi

A thesis
presented to the University of Waterloo
in fulfillment of the
thesis requirement for the degree of
Master of Science
in
Systems Design Engineering

Waterloo, Ontario, Canada, 2014

Author's Declaration

I hereby declare that I am the sole author of this thesis. This is a true copy of the thesis, including any required final revisions, as accepted by my examiners.

I understand that my thesis may be made electronically available to the public.

Majed Alghamdi

Abstract

In this work, novel electrostatic micro-electro-mechanical system (MEMS) sensor and sensors are introduced and demonstrated. First, a novel bifurcation-based MEMS ethanol vapor sensor is demonstrated. In contrast to traditional gas sensors that measure in analog mode (quantify) gas concentration, this sensor does not quantify the gas concentration. Rather, it detects its gas concentration in binary mode, reporting (1) for concentrations above a preset threshold and (0) for concentrations below the threshold. The sensing mechanism exploits the qualitative difference between the sensor state before and after the static pull-in bifurcation in electrostatic MEMS. The transition between these states is the bifurcation used in detection. A driving circuit with a resolution of 1 mV was used to drive the sensor at a point close to the pull-in limit to achieve maximum sensitivity. The sensor was able to detect concentrations as low as 5 ppm of ethanol vapor in dry nitrogen, equivalent to a detectable mass of 165 pg. Gas detection was verified electrically and optically through a detection circuit and a CCD camera, respectively.

Second, a novel tunable MEMS magnetic field sensor is demonstrated in this work. It measures torsional vibrations excited via Lorentz force. The sensor sensitivity and dynamic range can be tuned by varying a bias voltage. Experimental demonstration shows that the sensor sensitivity can be changed from 0.436 (mm/s)/mT at 6 V bias to 0.87 (mm/s)/mT at 1 V bias. Unlike most commercial magnetic sensors, this magnetic sensor achieves a higher bandwidth (182 kHz) and a tunable sensitivity adjustable on-the-fly.

Acknowledgements

First of all, I would like to thank my God for guiding and helping make everything possible while doing this work. I would like to express my deep appreciation to my supervisor, Prof. Eihab Abdel-Rahman for his guidance and help throughout this work. I am very grateful to him for spending a lot of time to review my thesis and the publications out of this work. Also, I would like to thank my co-advisors, Dr. Mahmoud Khater and Dr. Sangtak Park for their support, encouragement and for spending a lot of their valuable time for helping me throughout this work.

I would like to thank my thesis readers, Prof. Mustafa Yavuz and Prof. John Yeow for their comments and time in evaluating my work. I am very grateful to my colleagues Ahmad Kamal, Abdullatif Alwasel, Ayman Alneamy, Mohammad Attaher, Karim Alrayes, Reda Almikhlafi and Resul sarta for their cooperations and suggestions through this work. Also I would like to thank all my friends at University of Waterloo for their support and encouragement throughout my research study.

Special thanks to King Abdulaziz City for Science and Technology (KACST) for their scholarship and funding me during my Master degree.

I am extremely thankful to my parents for their sacrifices to help me reach this level of education. I am very grateful to my wife for her support, encouragement and patience throughout my study. My thanks also go to my brothers and sisters for their encouragement and support. Without them I could not be able to achieve it.

Thank you all so much.

Dedication

To my beloved father, Saleh

To my beloved mother, Azah

To my beloved wife, Shuruq

To my brothers, Mohammad, Hani and Emad

To my sisters, Maha, Manal, Tahani and Amani

and

To my beloved son, Saleh

Table of Contents

List of Tables **ix**

List of Figures **xi**

1 Introduction **1**

1.1 Inertial Sensors 1

1.2 Gas Sensors 4

1.3 Magnetic Sensors 7

1.4 Auther's Current Contribution 9

2 MEMS Gas Sensors **10**

2.1 Gas Sensor 10

2.1.1 Sensor design 10

2.1.2 Polymeric sensing materials 12

2.1.3 Electrostatic actuation 12

2.1.4 Detection mechanism 13

2.1.5 Drive/Detection circuit . . . 13
2.2 Sensor Model . . . 15
2.3 Sensitivity Analysis . . . 19
2.4 Parameter Identification . . . 22
2.4.1 Sensor dimensions . . . 22
2.4.2 Pull-in voltage . . . 23
2.4.3 Quality factor . . . 25
2.5 Experimental Limitations . . . 26
2.5.1 Static charge shock . . . 26
2.5.2 Dielectric charging . . . 27
2.5.3 Contact resistance . . . 28
2.5.4 Limitation of the detection circuit . . . 33
2.6 Experimental setup . . . 34
2.7 Results . . . 36
2.7.1 Ethanol detection using PANI-10% NiO . . . 37
2.7.2 Ethanol detection using P25DMA . . . 38
2.8 Discussion . . . 40

3 Magnetic Sensor **42**

3.1 Principle of Operation . . . 42
3.2 Numerical Model . . . 47

3.3 Experimental Results 48
3.3.1 Modal response 50
3.4 Sensor Demonstration 56
3.4.1 Forced mode 56
3.4.2 Resonant mode 57
3.5 Sensor Calibration 60
3.5.1 Calibration using a Gaussmeter 60
3.5.2 Calibration using a Hall Effect sensor 63

4 Conclusions and Future Work **71**

4.1 Binary Gas Sensor 71
4.2 Magnetic Field Sensor 72
4.3 Future Work 73
4.3.1 Dynamic Gas Sensor 73
4.3.2 Magnetic Field Sensor 73

References **74**

List of Tables

2.1 Sensor design dimensions 19

2.2 Measured sensor dimensions 22

2.3 Measured resistance and impedance for two sensors in area-contact 29

2.4 Measured resistance and impedance for three sensors in line-contact 31

2.5 Measured impedance and phase shift between microplate and bottom electrode doe three sensors 33

2.6 Measured resistance, impedance, and phase shift for a sensor pulled-in in area-contact 33

2.7 Experimental results for the PANI-equipped binary ethanol sensor (EtOH) 39

2.8 Experimental results for the P25DMA-equipped binary ethanol sensor (EtOH) 40

3.1 Bending mode excitation signals and their response 51

3.2 Torsional mode excitation signals and their response 53

3.3 Forced-mode sensing 56

3.4 Resonant-mode sensing 57

3.5 The peak amplitude in the FFT of the measured velocity at the microplate edge as a function of the magnetic field strength B for a bias voltage of $V_{dc} = 0$ V. 61

3.6 The peak amplitude in the FFT of the measured velocity at the microplate edge as a function of the magnetic field strength B for a bias voltage of $V_{dc} = 2$ V 62

3.7 Sensor sensitivity and noise equivalent field strength at seven operating points 69

List of Figures

2.1 A picture of the sensor under white light profilometer 11

2.2 Schematic of the driving/detection circuit 14

2.3 A schematic of the gas sensor 15

2.4 Nondimensional deflection of the plate center w_c as a function of V_{DC} . . . 20

2.5 Sensitivity S_m as a function of operating voltage $V_\circ$ 21

2.6 Plate center displacement w_c as a function of the actuation voltage $V_\circ$ obtained experimentally (solid line) and numerically (dashed line) 23

2.7 A screen capture of the laser vibrometer interface showing displacement of the plate center w_c (solid line) during pull-in. Superimposed is the actuation triangular wave (dashed line) 24

2.8 A screen capture of the laser vibrometer interface showing the FFT of the sensor frequency-response under a pulse train 25

2.9 A screen capture of the laser vibrometer interface showing the time response of the sensor under a pulse train 26

2.10 SEM pictures of the bottom electrode for sensors: (a) after seven pull-in cycles, (b) after three pull-in cycles, and (c) no pull-in 28

2.11 Pictures of (a) the unactuated sensor (0 V) and (b) the sensor in area-contact subsequent to pull-in 30
2.12 Electrical components of line-contact phenomena 31
2.13 Pictures of (a) the unactuated sensor and (b) the sensor in line-contact subsequent to pull-in 32
2.14 The gas sensor drive/detection circuit 34
2.15 The experimental setup 35
2.16 The test chamber is equipped with (a) quartz glass window and (b) a BNC port 36
2.17 PANI-equipped sensor (a) in area-contact after detection of 1000 ppm ethanol in dry nitrogen and (b) in line-contact after detection of 100 ppm ethanol in dry nitrogen 38

3.1 Isometric view of the magnetic sensor showing the excitation current (red dotted lines), the external magnetic field (green dashed line), and the Lorentz force (blue solid lines) 43
3.2 Top view (left) of the magnetic sensor and the microplate (right) color coded with measured displacement (red: high; green: low) when excited into torsional oscillations 45
3.3 (a) Top and (a) front views of the magnetic sensor 46
3.4 The first four undamped mode shapes of the magnetic sensor obtained from eigenfrequency analysis using COMSOL 48
3.5 Experimental set-up showing the laser vibrometer, probe station, micro manipulators, and specimen 49

3.6 Two measured points, A and B, for the bending and torsional modes . . . 51

3.7 The mode shape of the first out-of-plane bending mode obtained experimentally at $2f_\circ = 31$ kHz . . . 52

3.8 Comparison of the first out-of-plane bending mode shape obtained by (a) FEM at 34 kHz (b) and experimentaly at 31 kHz . . . 53

3.9 The first torsional mode shape obtained experimentally at $f_\circ = 182$ kHz . . 54

3.10 Comparison of the first torsional mode shape obtained by (a) FEM at 198 kHz and (b) experimentally at 182 kHz . . . 55

3.11 The FFTs of the measured velocity amplitude at point B in (a) the absence and (b) presence of an external magnetic field $B = 27.8$ mT when operated in forced-mode $f_\circ = 31$ kHz . . . 57

3.12 The FFTs of the measured velocity amplitude at point B in (a) the absence and (b) presence of an external magnetic field $B = 27.8$ mT when operated in resonant-mode $f_\circ = 182$ kHz . . . 58

3.13 Compassion between the FFTs of the sensors response to an external magnetic field $B = 27.8$ mT in (a) forced-mode ($f_\circ =$ 31 kHz) and (b) resonant-mode ($f_\circ =$ 182 kHz) operation . . . 59

3.14 The magnetic sensor mounted inside the Gaussmeter test chamber . . . 61

3.15 The calibration curves of the sensor for bias voltages of $V_{dc} = 0$ V (blue line) and $V_{dc} = 2$ V (red line) . . . 62

3.16 The magnetic sensor mounted inside the Hall effect test chamber . . . 63

3.17 (a) The area-grid and the line-grid $\overline{AC}$ used to measure the displacement and velocity of the microplate (b) Averaged frequency responses of the magnetic sensor excited by I_c= 3.3 mA sinusoidal current loop at 182 kHz with zero DC bias and external magnetic field of 64 mT 64

3.18 (a)The configuration of the sensor at phase angles $\phi = 0°, 90°$, and 270° within the torsional oscillations cycle.(b) The measured displacement of the grid point along line $\overline{AC}$ on the microplate at phase angles $\phi = 0°, 90°$, and 270° and (c) the measured displacement (blue solid lines) and velocity (red dashed lines) of points A, B, and C during a period of oscillations. Excitation current amplitude and frequency were set to I_p = 3.3 mA and $f_\circ$ = 182 kHz and the external magnetic field to B = 64 mT 66

3.19 The frequency-response of point A velocity for a sensor bias voltage of $V_{dc} = 0, 1, 2, 3, 4, 5$, and 6 V, when excited by a current with amplitude and frequency of I_p = 3.3 mA and $f_\circ$ = 182 kHz in a magnetic field of B = 64 mT (0 dB = 1 m/s) 67

3.20 The calibration curves of the magnetic sensor for seven operating points at $V_{dc} = 0, 1, 2, 3, 4, 5$ and 6 V 68

3.21 Measured velocity amplitude of point A as a function of bias V_{dc} for three levels of magnetic field strength 69

Chapter 1

Introduction

1.1 Inertial Sensors

A Micro-Electro-Mechanical Systems (MEMS) fabrication technology combine electrical and mechanical capabilities in one device at a very small scale, micro-scale $\propto 10^{-6}$m. It has the ability to produce devices that can mimic larger-scale devices performance which has shifted the way researchers, designers, and manufacturers think. It has introduced significant fabrication advantages, such as high-speed, high precision, small size, low cost and low power consumption, into the field of electronic and mechanical applications.

MEMS devices are mass produced which help bring down costs. The size and cost of the large scale devices has restricted there applications. The demand for low cost and small size technology is especially advantageous; for instance; surgeons may require micro forceps to perform intricate medical procedures. Size reduction of MEMS devices also allows for performance enhancements, such as integration of several sensors on the same die. The wide range of MEMS applications also stems from their improved sensitivity when deployed as sensors. MEMS have seen application in a wide range of fields, such as

automotive, chemical, medical, biological, safety, aviation, and telecommunication sectors, where they are well known consumer products today.

MEMS devices are predominately made of silicon which is a semiconductor that can deal easily with electrical signals. Most MEMS are fabricated using surface or bulk micromachining [1]. Surface micromachining process is a standard process based on patterning of thin film layers atop of the substrate. It depends on depositing and etching different film layers on the substrate to create MEMS structures. It is commonly utilized commercially in IC manufacturing [2]. Using surface micromachining, MEMS devices can be integrated with ICs on one chip, thereby enhancing their mechanical and electrical characteristics and further reducing their cost [1, 2].

Bulk micromachining is also a standard process depends on depositing thin film layers atop of the substrate and selectively etching the substrate to create MEMS structures. It is less expensive than surface micromachining because it involves a lower number of fabrication steps than surface micromachining. In addition, bulk micromachining is very useful for structures that need thicker substrates. Most commercially available MEMS pressure and inertial sensors are fabricated by bulk micromachining [1].

MEMS devices are transducers that transform one form of energy to another. They are classified into sensors or actuators depending on their application [3]. In this research, we focus on inertial sensors, which is the most commercially class of MEMS today. They include MEMS accelerometers, gyroscopes, magnetometer, and gas sensors [4, 2, 5]. The small size, low cost, and high performance of MEMS inertial sensors have allowed them to lead the market. Roben and Mounier [6] forecasted that the price of inertial sensors will drop by 40% to 60% over the next five years due to increased unit numbers and a rise of competition.

MEMS accelerometers have been widely used in automotive applications, such as seat belt control and air bag deployment [7, 2]. Accelerometers are designed to measure the acceleration of a body moving in space [1]. Many of them use a sprung proof mass to measure the acceleration along a signal axis [8]. For example, Jianbing et al. [9] introduced an accelerometer that determines acceleration along single planar axis by measuring the differential capacitance between two sets of parallel plates when the proof mass moves. It uses a thin SOI handle layer to enhance its sensitivity obtain a sensitivity of 2.25 V/g and a linearity of 0.5%. Accelerometers are also used in a broad range of applications, such as pedometers, earthquake detection, wii remote controllers, hard drive protection in laptops, and picture stabilization in camcorders [4, 2].

Gyroscopes represent another popular MEMS inertial sensor. They measure angular velocity and are commonly used in navigation systems [10, 2]. The operating principle of vibratory MEMS gyroscopes is to excite oscillations in a drive mode that interacts with a small rotation to produce, via Coriolis force, motions along a sense-mode [1]. Chen et al. [11] introduced a tuning fork gyroscope that uses a magnetic force to excite a drive-mode along the x-axis; when a rotation is introduced into z-axis, Coriolis force causes a change in the capacitance of a parallel plate capacitor aligned along the sense-mode direction (y-axis).

The small size of MEMS sensors has the advantage of allowing for integration, and thereby enhancing overall performance and offering new capabilities. Inertial Measurement Units (IMUs) are a prime example of this approach to sensing. They combine accelerometers, gyroscopes and magnetometers in one chip to measure a motion in space [12]. IMUs are used to measure translational acceleration along three axes and angular rotations around three axes as well as to reduce drift errors. For example, Ding et al. [13] introduced an IMU specifically designed for medical applications, such as tracking forearm

posture over time.

In this research effort, we address two categories of inertial sensors: gas sensors and magnetic sensors. The sensors considered here are based on novel operational principles that will be discuss in details in chapters 2 and 3.

1.2 Gas Sensors

Micro-mass sensors have been widely used as sensing platforms for inertial gas sensors in chemical, medical and automotive application [14, 15, 16]. The platform is coated by a detector material with high selectivity to a target gas. They detect the presence of the target gas in ambient air as a small variation in the sensor mass, on the order of nano- to atto-gram [14]. The response of gas sensors can be measured optically [17, 18, 19, 20, 16], capacitively [21], or piezoresistively [22, 23]. Optical readout is more accurate than other measurement techniques. MEMS gas sensors have been realized; however, they have significant challenges, such as stability, selectivity and sensitivity of the functional material, detection range, response time, hysteresis, power consumption, reliability and cost effectiveness [24, 15].

There are two commonly used detection techniques in gas sensors, which are static and dynamic sensing modes. The static mode measures variation in mass as a change in structural displacement. Jensenius et al. [22] used a pezioresistor to monitor the static deflection of a microcantilever obtained a minimum detectable concentration of 10 ppm of alcohol vapour in dry nitrogen. A Wheatstone bridge was used to measure the change in the voltage across the piezoresistor before and after detection of alcohol. Zhu et al. [23] used a piezoresistor to measure the static deflection of a V-shaped cantilever beam equipped by a layer TTF-C4P to detect trinitrobenzene vapour. They obtained a minimum detectable

concentration of 10 ppb of trinitrobenzene vapour in dry of nitrogen. Datskos and Sauers [17] employed static sensing of a gold-coated microcantilever to detect 2 mercaptoethanol vapour in dry of nitrogen. The lowest concentration detected optically was 65 ppb.

In dynamic sensing mode, the sensor measures the shift in one of its resonant frequencies induced by a mass sorbed onto a detector material due to the presence of a target gas in ambient air. This sensitivity of this sensing mode is higher than that of static or forced response sensing by 1-2 order of magnitude [25, 26]. Therefore, it has the ability to increase absolute mass detection capabilities and can be utilized as highly sensitive biological sensors, enabling single cell, virus, and double-stranded DNA molecule detection [27].

Park et al. [16] introduced a mass sensor to monitor the evaporation of microdroplets of water and dimethyl sulfoxide (DMSO). They measure the change in a membrane's natural frequency induced by the change in the magnitude of the added mass as it varies during evaporation. Zribi et al. [15] presented a sensor that detects humidity level and carbon dioxide concentration by measuring the shift in the natural frequency of a coated membrane. They measured a minimum resolution of 1 ppm of water vapor and 0.7% vol of CO_2 in dry nitrogen. Dohn et al. [21] presented an electrostatic microcantilever mass sensor that measures added mass by detecting the change in the beam resonant frequency. The frequency shift is measured as the time-averaged current obtained from intermittent contact, during oscillations, between the cantilever beam and an electrode. This method was reported to reduce system noise and enhance detection of the frequency shift to a resolution of 1/80000 in ambient conditions. IIic et al. [14] introduced a nanocantilever detector that can detect a virus by measuring a shift in resonance frequency corresponding to its mass. They experimentally achieved a minimum detectable mass of 3 fg.

Dufour et al. [28, 29] investigated the effect of the sensor mode shapes on its quality

factor in gas and liquid media. Three vibrational modes of a microcantilever beam sensor were studied: in-plane (lateral) bending, out-of-plane (transverse) bending, and elongation (axial). They compared experimentally the quality factor for each mode in air and three liquids and found that the quality factor of the out-of-plane bending mode is one-order of magnitude higher in air than in liquids. In liquids, the quality factor of the in-plane bending mode was two-orders of magnitude higher than that of the out-of-plane bending mode. They showed that the dominant effect responsible for reducing the quality factor of the out-of-plane bending mode in liquids was hydrodynamic forces.

We note that most of the static and dynamic sensors described, thus far, are made of cantilever beams. This is because the sensitivity of an inertial sensor is proportional to its structural compliance [19, 18, 20, 21], which is particularly high in cantilever beams.

A special class of inertial sensors seeks to use nonlinearities and the bifurcation they cause to enhance sensor sensitivity [30, 31, 5]. Zhang et al. [25, 32] showed that the sensitivity of an electrostatic MEMS mass sensor is highly increased by replacing the traditional frequency shift measurand, the natural frequency, with the bifurcation point of a subcritical pitchfork bifurcation resulting from principle parametric resonance. They used platinum to detect water vapour and measured a minimum mass of 0.7 pg water vapour. Yie et al. [33] developed a parametric amplification technique that can be used to achieve high quality factor and, thereby, enhance the sensor sensitivity. They showed experimentally enhancement in the quality factor of their mass sensor at atmospheric pressure when parametric amplification was implemented.

Younis and Alsaleem [26] introduced two analogue microcantilever-based electrostatic MEMS sensors that measure added mass as a shift in bifurcation point of a cycle-fold bifurcation due to primary resonance and subcritical pitchfork bifurcation due to the subharmonic resonance of order one-half. They measured a minimum detectable mass of

1.07 μg corresponding to a frequency shift of 0.7 Hz. Kumar et al. [34] demonstrated the feasibility of a bifurcation-based piezoelectric sensor to detect methanol in dry nitrogen using poly(4-vinyl pyridine). It utilizes the frequency shift in the location of a cyclic fold bifurcation due to primary resonance. Harne et al. [35] demonstrated the feasibility of a mass sensor that detects added mass through the shift in the location of cyclic-fold bifurcation in the vicinity of primary resonance of a bistable beam.

Nayfeh and co-workers [31, 30] proposed two types of binary sensors based electrostatic MEMS: a static sensor and a dynamic sensor. The static sensor is actuated by DC voltage, whereas the dynamic sensor adds an AC component. The measurands of the static and dynamic sensors are the frequency shift in the location of a saddle node bifurcation and a cyclic-fold bifurcation, respectively. In this research effort, we develop a novel gas sensor that can detect ethanol in dry nitrogen based on the static binary sensing technique.

1.3 Magnetic Sensors

Magnetic sensors are indispensable in many industrial applications. The demand for magnetic sensors is increasing, especially in electronic compasses and navigation systems [36]. Most commercially available magnetic sensors are based on anisotropic magneto-resistance (AMR) or Hall effect. AMR sensors have higher sensitivity, smaller dynamic range, better thermal stability, and lower DC offset than Hall effect sensors [37]. On the other hand, Hall effect sensors have a wider bandwidth and are immune to hysteresis and saturation phenomena that limit the performance of AMR sensors [38]. To avoid these limitations, research has focused on development of MEMS magnetic sensors based on the Lorentz force. However, the sensitivity of these sensors is relatively low. Hence, most of them operate at resonance to take advantage of dynamic amplification [38, 39].

The Lorentz force resulting from interaction between current and magnetic field is used in MEMS magnetic sensors to excite bending [38, 40, 41] and torsional [42] modes of vibration. Piezoresistors [39, 43] and capacitors [36, 44, 38] are then used to measure the resulting strain and displacement, respectively. Langfelder et al. [45] compared the use of parallel-plate, comb-finger and fringe-field capacitance in measuring vibrations due to external magnetic fields. They found that fringe-field sensing has higher sensitivity and quality factor than parallel-plate or comb-finger sensing under the same experimental setup and on the same die. Frangi et al. [46] found that introducing holes into the stator in a comb-finger capacitor reduces mechanical dissipation and, hence, increases the resolution of its capacitive sensing. Their results show that optimizing the holes in the stator electrodes increases the sensitivity up to four times beyond a regular comb-finger to reach 4.5 aF/(μT mA) at 1 mbar.

Kádár et al. [47] introduced a magnetic sensor made of a coil placed on top of a plate to excite its torsional mode via Lorentz force at 2.5 kHz. The sensor was placed inside a vacuum chamber (5 Pa) to increase its quality factor to $Q = 700$. Its sensitivity and bandwidth were measured as 400 mV/μT and 20–25 Hz, respectively. Li et al. [42] presented a comb-finger magnetic sensor exploiting the first torsional mode of a beam at 21.29 kHz. Its resolution was measured 210 nT/$\sqrt{Hz}$ in a magnetic field of 450 μT. Stifter et al. [48] introduced a magnetic sensor made of a U-shaped cantilever beam resonating at 4.36 kHz in its first out-of-plane bending mode. They used two techniques to measure the magnetic field strength: a laser vibrometer to measure out-of-plane displacement and two electrodes to measure the displacement capacitively. The sensor resolution was reported to be 15 nT$\sqrt{Hz}$.

The small size of MEMS magnetometers allow multi-axis magnetometers that measure magnetic field strength using one magnetometer per axis on the same chip [36, 40, 41, 44].

Chang et al. [38] presented a CMOS-MEMS resonant magnetic sensor to measure magnetic field strength along an in-plane and an out-of-plane axes. The in-plane magnetic coil is fabricated from metal/tungsten layers by using TSMC 0.35 m 2P4M process. They measured a resolution of 296.5nT/$\sqrt{Hz}$ along the in-plane axis and a resolution of 121.6 nT/$\sqrt{Hz}$ along the out-of-plane axis.

In this research effort, we develop in chapter 3 a novel magnetometer that can detect magnetic field strength via Lorentz force.

1.4 Auther's Current Contribution

My contribution in this work include experimental and analytical studies to compare the sensor performance to previous predictions reported in Khater [49]. I carried out this work under the supervsion of Dr. M. Khater, and S. Park, in addition to professor E. Abdel-Rahman. I hereby acknowledge that a part of the work presented in Chapter 2 and Chapter 3 have been published and adapted from:

- M. E., Khater, M., Al-Ghamdi, S., Park, K. M. E. Stewart, E. M. Abdel-Rahman, A. Penlidis, A. H. Nayfeh, A. K. S. Abdel-Aziz, and M. Basha. "Binary MEMS gas sensors," Journal of Micromechanics and Microengineering, vol. 24, pp. 065007/1-9, 2014.

- S., Park, M., Al-Ghamdi, M., Khater, M. E., E. M., Abdel-Rahman, M., Yavuz, "Adjustable sensitivity MEMS magnetic sensor," ASME International Design Engineering Technical Conferences, 2014.

Chapter 2

MEMS Gas Sensors

Binary gas sensors detect the presence of a target gas in its vicinity in a binary fashion. Compared to commercial sensors which quantify the concentration of a gas in analog mode, a binary gas sensor does not measure the concentration of the gas. Rather, it indicates the state of gas concentration using a discrete signal with two states only: '1', above a threshold, and '0', below it. The electrostatic pull-in phenomenon is exploited here to create those discrete (binary) output states.

2.1 Gas Sensor

2.1.1 Sensor design

The sensor was fabricated using the PolyMUMPs fabrication process [50]. It features two cantilever beams, 125 × 5 × 1.3 μm, supporting a 30 × 60 × 1.3 μm sense-plate where a detector polymer is placed. The structure is fabricated in Poly2 structural layer. A polysilicon electrode is patterned on the substrate directly under the sense-plate, out of

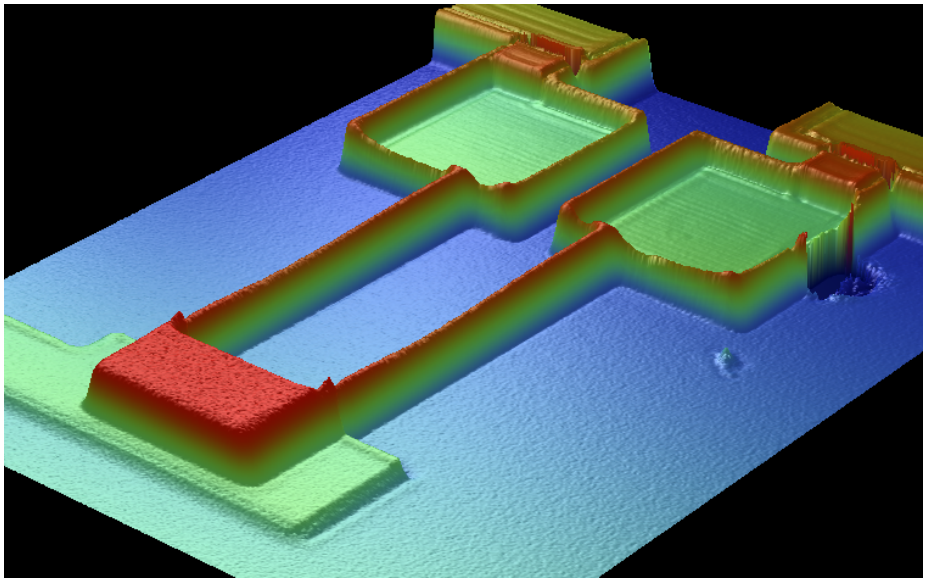

Figure 2.1: A picture of the sensor under white light profilometer

layer Poly0, to act as ground for the electrostatic field, Fig. 2.1. The beams attach to the plate on both sides in order to maximize torsional stiffness. Two gold pads are patterned at the roots of the support beams to apply potential difference between the plate and the substrate electrode. The pads are also used to drive a current through the semi-conductive polysilicon structure to reset the sensor via Joule heating.

The following design criteria and constraints were used in developing the sensor:

- Maximize the sense-plate to increase the surface area used to deposit the detector polymer and decrease the actuation voltage.
- Maximize the distance between the two actuation electrodes and the ground electrode to reduce leakage current.
- Minimize the cantilever beams cross-sectional dimensions to reduce the sensor stiff-

ness and, therefore, reduce the actuation voltage.

- Eliminate release holes to prevent polymer solution leakage during deposition.

2.1.2 Polymeric sensing materials

Two different polymeric sensing materials with affinity to ethanol vapor, polyaniline doped with 10% weight nickel oxide (PANI-10% NiO) and poly 2,5-dimethyl aniline (P25DMA), were deposited onto separate sensors [51]. Each polymer was dispersed in a 1% solution of glycerol. Glycerol was used to facilitate deposition since it did not completely wet the surface of the sense-plate, thereby keeping the polymer solution from running off the plate edge. An average of three drops of the polymer-glycerol solution were deposited onto each sense-plate. The glycerol was then evaporated off in air, leaving the polymers on the sense-plate. The sensors, with their respective sensing materials, were then evaluated for sensitivity towards ethanol.

2.1.3 Electrostatic actuation

The binary gas sensor employs electrostatic actuation, applying a voltage difference between a moving and a fixed plate, an attraction force is developed resulting in moving the two plates towards each other [1, 52]. Electrostatic actuation is widely-used in MEMS where it provides the least power requirements amongst all actuation techniques, since its current requirements are minimal. Further, electrostatic actuation provides high energy density and a well-regulated force over small, micro-sized, perturbations [52]. Moreover, electrostatic actuation does not put significant restrictions on the sensor design process, thus providing for a lower cost and simpler fabrication process and operating conditions compared to other actuation methods.

2.1.4 Detection mechanism

Pull-in instability technique is used in this project as a binary logic where the system can either, detect '1' or not detect '0', the gas of interest in vicinity. When the sensor is actuated using a DC voltage, it responds by a static deflection of the sense-plate. The sense-plate collapses onto the fixed electrode when the DC voltage exceeds a 'pull-in' voltage V_p. The sensor is excited at a point that is very close to pull-in, namely, saddle node bifurcation. The sensing mechanism exploits the qualitative difference between the sensor-state before and after pull-in. The transition between these two states is the static bifurcation used in detection. The two qualitatively different sensor states, before and after pull-in, serve as the binary sensor states representing the state of a gas concentration in air.

Applying an operating voltage $V_\circ$ close to the pull-in voltage, the mass added by ethanol molecules sorbed to the detector polymer will cause the sense-plate to collapse onto the substrate when it reaches a critical value. As the concentration of the target gas in air increases, the number of gas molecules captured by the detector polymer will increase until their 'added mass' reaches that critical value. The magnitude of the set-off voltage, $\delta V = V_{\text{pi}} - V_\circ$, determines the size of the critical mass and the threshold concentration above which ethanol in air triggers a detection signal; pull-in. The difference between the sensor impedance before and after pull-in is used as a metric to electrically detect ethanol concentrations above the threshold level.

2.1.5 Drive/Detection circuit

Stabilizing the operating voltage $V_\circ$ is necessary to reduce the sensor noise floor. A PC-controlled low-noise, high-precision, driving circuit was designed by Dr. Park [53] to regulate the actuation voltage. A USB-to-Serial converter connects the PC to a micro-controller

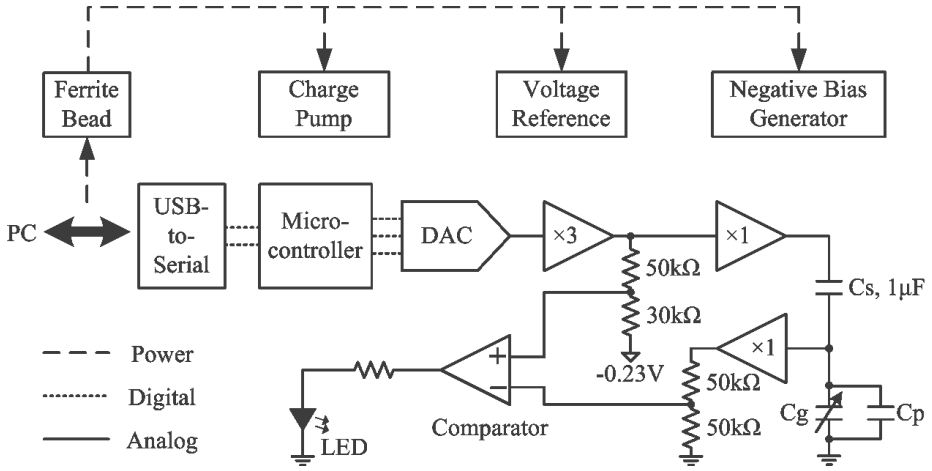

Figure 2.2: Schematic of the driving/detection circuit

and powers a circuit board. The micro-controller passes user commands to a Digital-to-Analog Converter (DAC). A voltage reference supplies the DAC with a low noise reference voltage of 4.096 V resulting in a DAC resolution of 62.5 μV. A non-inverting amplifier with a gain of 3 increases the actuation voltage range to $[0 - 11.7]$ V, which is then buffered by an operational amplifier. A charge pump supplies a voltage of 12 V to the amplifier and buffer, while a negative bias generator supplies them with a negative power rail of -0.23 V to allow their output voltage to reach down to 0 V. The measured resolution of the actuation circuit is 250 μV.

The contact detection circuit is composed of a buffer to minimize loading, a comparator to compare a measured actuation voltage against a commanded actuation voltage, and a LED to indicate contact. The gas sensor is connected to the high impedance non-inverting input of the buffer, which is used to measure the actuation voltage of the gas sensor and has very low input bias current (10 fA).

When the sense-plate touches the bottom electrode, contact introduces a shunt resis-

tance to a capacitive voltage divider, draining charge from the gas sensor and reducing the voltage of the gas sensor. When its voltage drops below a threshold value, the comparator changes its output from logic low to logic high, turning on the LED in order to indicate the contact. The block diagram of the low noise, high precision drive circuit and the contact detection circuit is presented in Fig. 2.2.

2.2 Sensor Model

The gas sensor [30, 49, 53] is made of an electrostatic MEMS actuator, a sense-plate supported by a microcantilever beam, as shown in Fig. 2.3. The plate is coated with a detector polymer, coupled to an electrode located at a distance d underneath it, and actuated by DC voltage. The detection mechanism is built on sensing the change in the location of a static bifurcation point due to an added mass (sorbed ethanol molecules) to the plate.

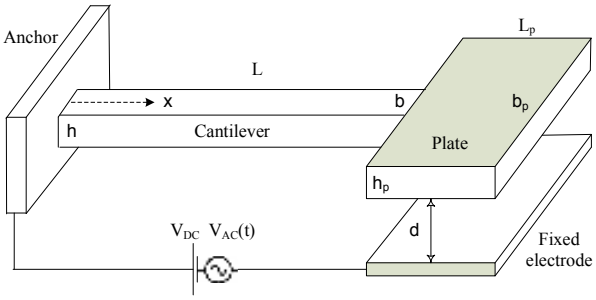

Figure 2.3: A schematic of the gas sensor

We adopt the model developed by Nayfeh et al. [54] for electrostatic MEMS gas sensors. The model is extended to account for the weight of the sense-plate, detector polymer, and

added-mass. It treats the microbeam as an elastic continuum, an Euler-Bernoulli beam, and the plate as a rigid body. The beam width, thickness, cross-sectional area, and moment of area are denoted b, h, A, and I, respectively. The micro plate mass and mass moment of inertia per unit length are denoted $\hat{m}_p$ and $J_c = \frac{1}{3}\hat{m}_p\hat{L}_c^2$. The subscript c stands for the center of mass of the plate and $\hat{L}_c$ is the distance from the beam end to the center of mass. The sensor equation of motion is derived using Hamilton's principle as [55, 54, 49]:

$$\rho A\ \ddot{\hat{w}}(\hat{x},\hat{t}) + c\ \dot{\hat{w}}(\hat{x},\hat{t}) + EI\ \hat{w}^{iv}(\hat{x},\hat{t}) = 0 \tag{2.1}$$

subject to the boundary conditions:

$$\hat{w}(0,\hat{t}) = 0 \qquad , \qquad \hat{w}'(0,\hat{t}) = 0 \tag{2.2}$$

$$\begin{aligned} EI\hat{w}''(L,\hat{t}) = {} & \hat{m}_p g\hat{L}_c - \hat{m}_p\hat{L}_c\ddot{\hat{w}}\left(L,\hat{t}\right) - \left(\hat{m}_p\hat{L}_c^2 + J\right)\ddot{\hat{w}}'(L,\hat{t}) + \frac{\varepsilon b_p(V_{\mathrm{DC}}+V_{\mathrm{AC}})^2}{2\hat{w}'^2(L,\hat{t})} \\ & \left[\frac{2\hat{L}_c\hat{w}'(L,\hat{t})}{d-\hat{w}(L,\hat{t})-2\hat{L}_c\hat{w}'(L,\hat{t})} - \ln\frac{d-\hat{w}(L,\hat{t})}{d-\hat{w}(L,\hat{t})-2\hat{L}_c\hat{w}'(L,\hat{t})}\right] \end{aligned} \tag{2.3}$$

$$\begin{aligned} EI\hat{w}'''(L,\hat{t}) = {} & \hat{m}_p\ddot{\hat{w}}(L,\hat{t}) + \hat{m}_p\hat{L}_c\ddot{\hat{w}}'(L,\hat{t}) - \hat{m}_p g - \frac{\varepsilon b_p\left(V_{\mathrm{DC}}+V_{\mathrm{AC}}\right)^2}{2\hat{w}'(L,\hat{t})} \\ & \frac{2\hat{L}_c\hat{w}'(L,\hat{t})}{(d-\hat{w}(L,\hat{t}))(d-\hat{w}(L,\hat{t})-2\hat{L}_c\hat{w}'(L,\hat{t}))} \end{aligned} \tag{2.4}$$

where $\hat{w}(x,t)$ is the displacement of the beam, d is the unactuated gap between the plate and the substrate, and $\hat{c}$ is the viscous damping coefficient. The overdot stands for the derivative with respect to time $\hat{t}$ and the prime stands for the derivative with respect to position along the beam axis $\hat{x}$.

For convenience, we introduce the nondimensional variables

$$w = \frac{\hat{w}}{d}, \qquad x = \frac{\hat{x}}{L}, \qquad t = \frac{\hat{t}}{T} \tag{2.5}$$

where T is a time scale. Substituting Eq. (2.5) into Eqs. (2.1) and (2.2), we obtain the

nondimensional equation of motion in the form

$$\ddot{w}(x,t) + c\,\dot{w}(x,t) + w^{iv}(x,t) = 0 \tag{2.6}$$

subject to the boundary conditions

$$w(0,t) = 0 \qquad , \qquad w'(0,t) = 0 \tag{2.7}$$

$$\begin{aligned} w''(1,t) = {} & M_p L_c - M L_c \ddot{w}(1,t) - \frac{4}{3} M L_c^2 \ddot{w}'(1,t) + \frac{\alpha (V_{\mathrm{DC}} + V_{\mathrm{AC}})^2}{w'^2(1,t)} \\ & \left[\frac{2 L_c w'(1,t)}{1 - w(1,t) - 2 L_c w'(1,t)} - \ln \frac{1 - w(1,t)}{1 - w(1,t) - 2 L_c w'(1,t)} \right] \end{aligned} \tag{2.8}$$

$$\begin{aligned} w'''(1,t) = {} & - M_p + M \ddot{w}(1,t) + M L_c \ddot{w}'(1,t) \\ & - \frac{2\alpha (V_{\mathrm{DC}} + V_{\mathrm{AC}})^2}{w'(1,t)} \, \frac{L_c w'(1,t)}{(1 - w(1,t))(1 - w(1,t) - 2 L_c w'(1,t))} \end{aligned} \tag{2.9}$$

where

$$\alpha = \frac{\varepsilon b_p L^4}{2 E I d^3}, \quad T = \sqrt{\frac{\rho A L^4}{E I}}, \quad c = \frac{\hat{c} L^4}{E I T}, \tag{2.10}$$

$$L_c = \frac{\hat{L}_c}{L}, \quad M = \frac{\hat{m}_p}{\rho A L}, \quad \text{and} \quad M_p = \frac{\hat{m}_p g L^3}{E I d} \tag{2.11}$$

and M_p is the nondimensional plate weight.

We proceed to develop a closed-form expression for the static deflection, denoted $w_s(x)$, under DC voltage and estimate the maximum range of travel. The static problem can be formulated by setting the time derivatives and the AC forcing term in Eqs. (2.6) and (2.7) equal to zero, which yields

$$w_s^{iv}(x) = 0 \tag{2.12}$$

subject to the boundary conditions

$$w_s(0) = 0 \qquad , \qquad w_s'(0) = 0 \tag{2.13}$$

$$w_s''(1) = M_p L_c + \frac{\alpha V_{\rm DC}^2}{w_s'(1)^2} \left[\frac{2L_c w_s'(1)}{1 - w_s(1) - 2L_c w_s'(1)} - \ln \frac{1 - w_s(1)}{1 - w_s(1) - 2L_c w_s'(1)} \right] \tag{2.14}$$

$$w_s'''(1) = -M_p - \frac{2\alpha V_{\rm DC}^2}{w_s'(1)} \frac{L_c w_s'(1)}{(1 - w_s(1))(1 - w_s(1) - 2L_c w_s'(1))} \tag{2.15}$$

where the primes denote derivatives with respect to x.

The general solution of Eq. (2.12) can be expressed as

$$w_s(x) = A\,x^3 + B\,x^2 + C\,x + D \tag{2.16}$$

Using the first two boundary conditions yields $C = D = 0$. The last two boundary conditions result in the following nonlinear algebraic equations:

$$6A + 2B = M_p L_c + \frac{\alpha V_{\rm DC}^2}{(3A + 2B)^2} \left[\frac{2L_c(3A + 2B)}{1 - A - B - 2L_c(3A + 2B)} - \ln \frac{1 - A - B}{1 - A - B - 2L_c(3A + 2B)} \right] \tag{2.17}$$

$$6A = -M_p - \frac{2\alpha V_{\rm DC}^2}{3A + 2B} \frac{L_c(3A + 2B)}{(1 - A - B)(1 - A - B - 2L_c(3A + 2B))} \tag{2.18}$$

which can be numerically solved for A and B.

The sensor structural material is polysilicon with $\rho = 2300$ Kg/m^3 and $E = 160$ GPa. The air permittivity is $\varepsilon = 8.854 \times 10^{-12}$ F/m. The design dimensions of the sensor are listed in Table 2.1.

Figure 2.4 shows the variation of the static deflection, $w_c = w_s(1) + L_c\, w_s'(1)$, of the plate center of mass with the DC voltage obtained by solving Eqs. (2.17) for a given $V_{\rm DC}$ and substituting the resulting values of A and B into Eq. (2.16). The pull-in voltage

Table 2.1: Sensor design dimensions

L (μm)	b (μm)	h (μm)	L_p (μm)	b_p (μm)	h_p (μm)	d (μm)
125	5	1.5	60	30	1.5	2.75

was calculated as $V_{\text{pi}} = 6.98$ V with plate deflection at pull-in, w_{pi}, equal to 32% of the initial gap d as depicted in the figure. The lower branch of solutions (solid line) represents stable equilibrium solutions, whereas the upper branch of solutions (dashed line) represents unstable equilibrium solutions. The two branches of solutions collide at this point, resulting in their destruction due to a saddle-node bifurcation. Beyond V_{pi}, there are no equilibrium positions [56].

2.3 Sensitivity Analysis

The sensitivity of static-detection sensors is defined as the ratio of the change in normalized deflection δw to the change in normalized mass δm

$$S_m = \frac{\delta w}{\delta m} \tag{2.19}$$

For an un-actuated sensor, this reduces to a constant value

$$S_m = \frac{\gamma}{k}$$

where γ is a normalization constant and k is the linear structural stiffness.

For actuated electrostatic sensors, the structural stiffness is function of the actuation voltage and, therefore, sensitivity will vary with voltage. Thus, we develop a closed-form sensitivity formula for static-detection electrostatic MEMS sensors. For a sensor set at an

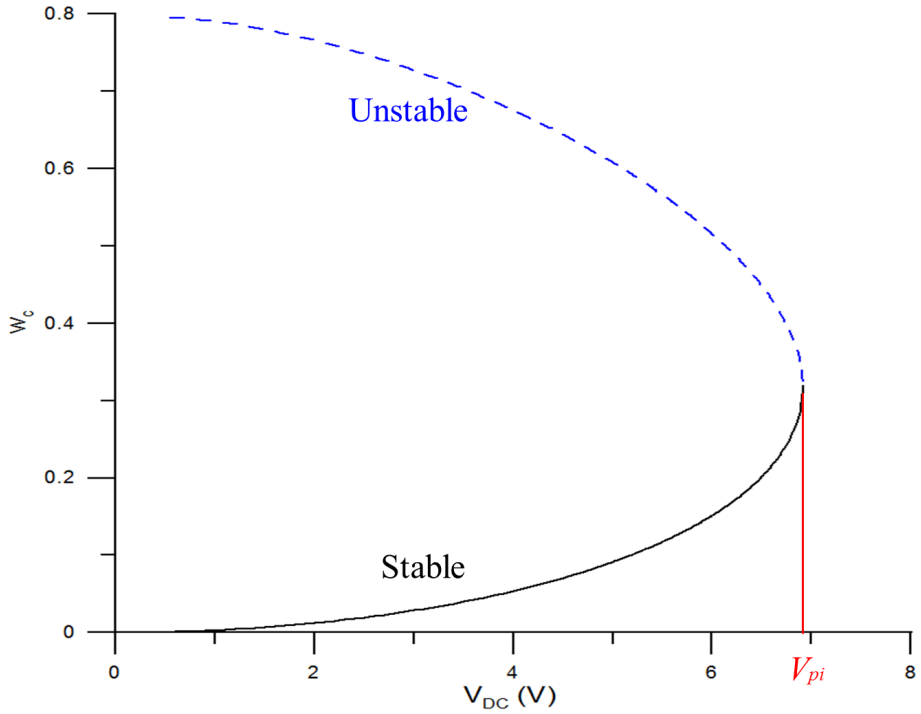

Figure 2.4: Nondimensional deflection of the plate center w_c as a function of V_{DC}

operating voltage $V_\circ$, we perturb the plate mass by δm and use Eq. (2.16) and Eqs. (2.17) to evaluate the perturbed plate deflection $w_c + \delta w$ and write

$$\delta w = (1 + 3L_c)\,\delta A + (1 + 2L_c)\,\delta B \tag{2.20}$$

Substituting this equation into Eq. (2.19), we obtain

$$S_m = (1 + 3L_c)\,\frac{\delta A}{\delta m} + (1 + 2L_c)\,\frac{\delta B}{\delta m} \tag{2.21}$$

The perturbed deflection coefficients are determined by solving Eqs. (2.17) analytically [49] to obtain

$$S_m = \frac{12\alpha V_\circ^2 \mathrm{L_c}(1 + \mathrm{L_c})(\mathrm{A} + \mathrm{B}) + 18\mathrm{L_c} + 10}{16\alpha V_\circ^2 \mathrm{L_c}(1 + 3\mathrm{L_c} + 3\mathrm{A} + 3\mathrm{B}) - 12} \tag{2.22}$$

where terms of order $O(\epsilon^3)$ and higher have been neglected. The formula indicates that sensitivity is not only function of compliance, represented by L_c, but also the strength of the electrostatic field, represented by $\alpha V_\circ^2$.

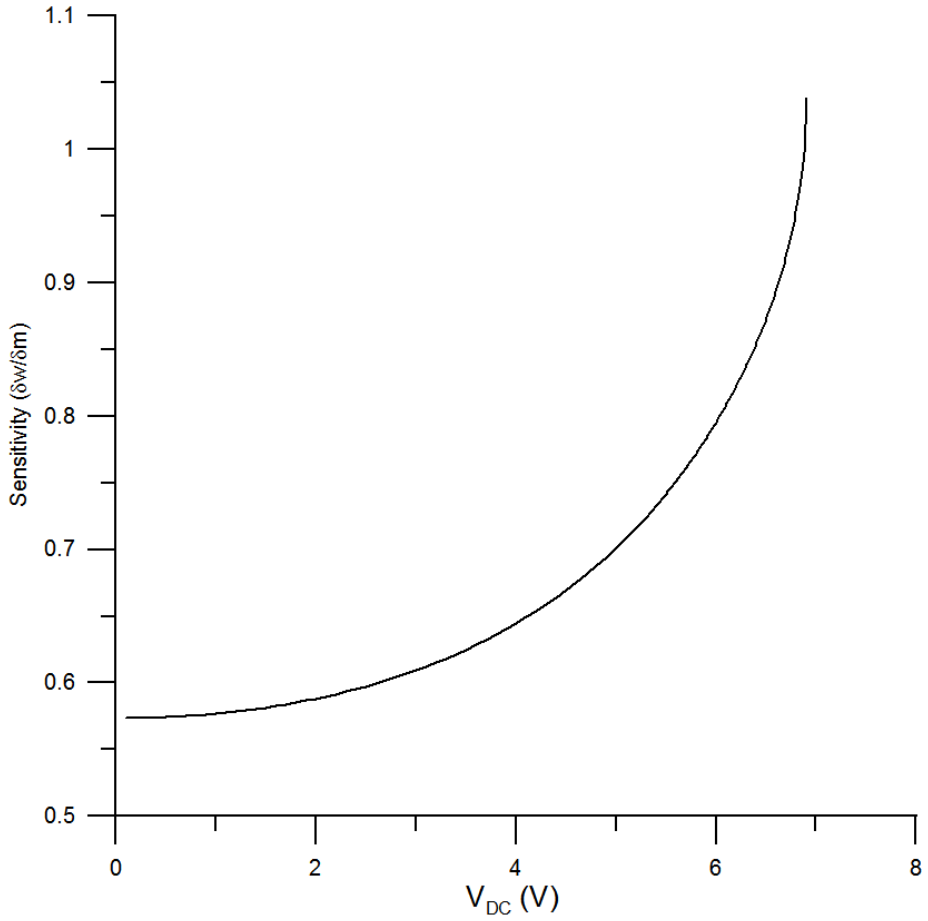

Figure 2.5: Sensitivity S_m as a function of operating voltage $V_\circ$

We solved Eq. (2.21) numerically to calculate the sensitivity of the sensor as a function of the operating voltage $V_\circ$, Fig. 2.5. Our results show that sensitivity increases monotonically with $V_\circ$ and approaches a maximum as $V_\circ \to V_{\text{pi}}$. This is in agreement with Eq. (2.19)

since static pull-in corresponds to the sensor linear stiffness approaching zero ($k \to 0$). Therefore, it is advantageous to use electrostatic MEMS sensors and to operate them as close as possible to the pull-in limit. In fact, the sensitivity of a binary mass sensor operated by triggering pull-in, represents an upper bound on the sensitivity of static-detection electrostatic MEMS sensors.

2.4 Parameter Identification

2.4.1 Sensor dimensions

Uncertainties in the large in-plane dimensions of the sensor are insignificant compared to uncertainties in the small capacitor gap distance, structural layer thickness, and width of the cantilever beams. We used a white light profilometer [57] to measure the in-plane dimensions of the beams and sense-plate as listed in Table 2.2. We found that they are almost identical to the design values except for the beam width which was found to be $b = 5.5$ μm.

Table 2.2: Measured sensor dimensions

L (μm)	b (μm)	h (μm)	L_p (μm)	b_p (μm)	h_p (μm)	d (μm)
124	5.5	1.3	60	30	1.3	2.15

In order to estimate the beam thickness, we matched the voltage-displacement curve predicted by our model to that measured experimentally as shown in Fig. 2.6. The beam thickness required to obtain matching between the experiment and model predictions was $h = 1.3$ μm. Moreover, Fig. 2.6 also gives an estimate of the capacitor gap distance as

$d = 2.15$ μm. The close agreement between model and experimental results indicate that the model predicts well the sensor displacement until pull-in.

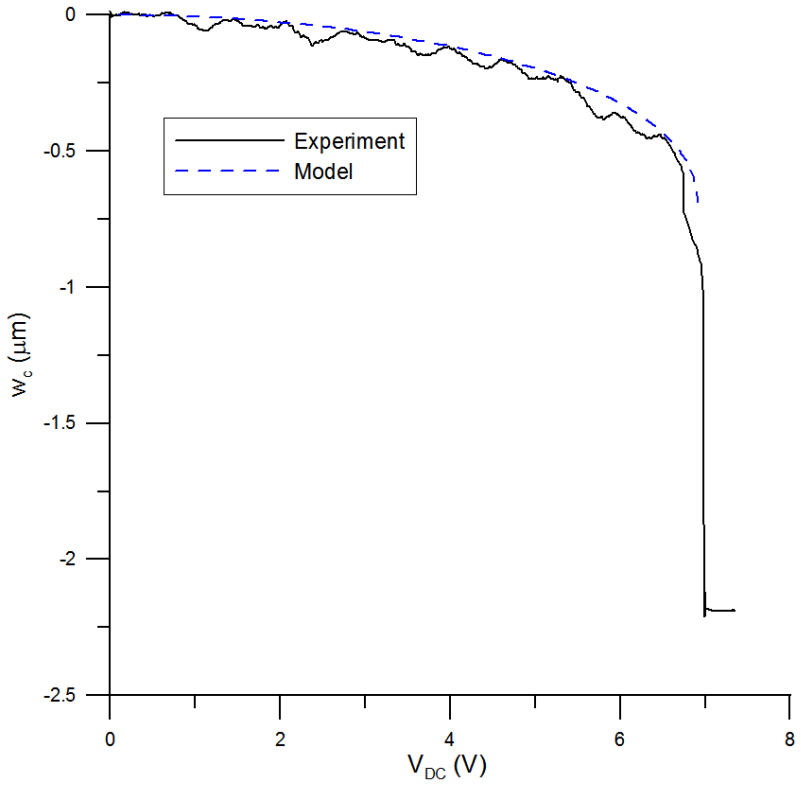

Figure 2.6: Plate center displacement w_c as a function of the actuation voltage $V_\circ$ obtained experimentally (solid line) and numerically (dashed line)

2.4.2 Pull-in voltage

A laser vibrometer [58] is used to measure the sensor response. It uses the difference in a laser beam frequency and phase before and after it reflects from the plate center to determine the sensor displacement w_c and velocity $\dot{w}_c$.

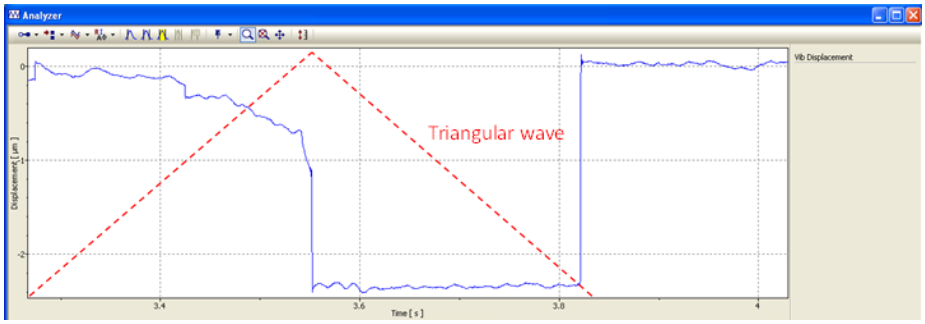

Figure 2.7: A screen capture of the laser vibrometer interface showing displacement of the plate center w_c (solid line) during pull-in. Superimposed is the actuation triangular wave (dashed line)

In order to determine the pull-in voltage, a triangular wave is applied to the sensor using the driving circuit. The frequency of the triangular wave is set to 3 Hz to ensure a quasi-static response. The maximum voltage of the waveform is monotonically increased until pull-in occurs. Pull-in is detected via the vibrometer as a sudden change in the plate deflection. It is verified optically by the formation of alternating bright and dark fringe fields on the cantilever and sense-plate and electrically by the contact LED of the detection circuit turning on.

A screen capture from the laser vibrometer interface, Fig. 2.7, shows a picture of the laser spot positioned over the sense-plate and the measured plate displacement over time in response to a triangular wave varying from 0 - 7 V at a frequency of 3 Hz. As the voltage increases linearly, the plate moves down towards the substrate. It undergoes pull-in at the peak of the triangular wave and stays in contact with the substrate as the voltage drops until it approaches 0 V.

This experimental procedure provides an estimate of the pull-in voltage accurate up to 0.1 V due to residual dynamic effects caused by the time-varying voltage of the triangular

wave. To obtain a better estimate of the pull-in voltage, an operating voltage $V_\circ$ close to but less than the estimated pull-in voltage is applied to the sensor. The voltage $V_\circ$ is increased in steps of 1 mV, allowing transients to die out after each step, until pull-in occurs. This procedure provides an enhanced estimate of the pull-in voltage accurate up to 1 mV.

2.4.3 Quality factor

We measured the quality factor of the sensor in atmospheric pressure by applying a pulse train with an amplitude of 4 V, a frequency of 1 kHz, and a 5% duty cycle. Using laser vibrometer, we obtained the frequency-response curve of the sensor, Fig. 2.8. The damped natural frequency was measured from the curve as $f_d = 24$ kHz. The quality factor was determined from the curve using the half-power bandwidth method as $Q = 0.92$ indicating that the sensor is highly damped. We also measured the settling time from the time-domain response to the pulse train as $t_s = 20$ μs shown in Fig. 2.9.

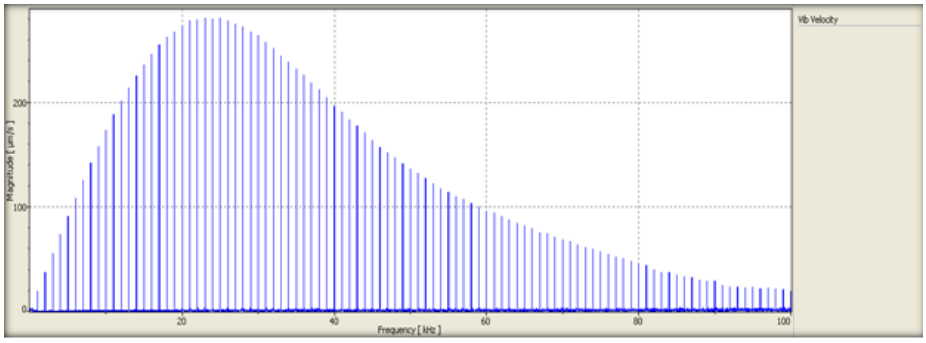

Figure 2.8: A screen capture of the laser vibrometer interface showing the FFT of the sensor frequency-response under a pulse train

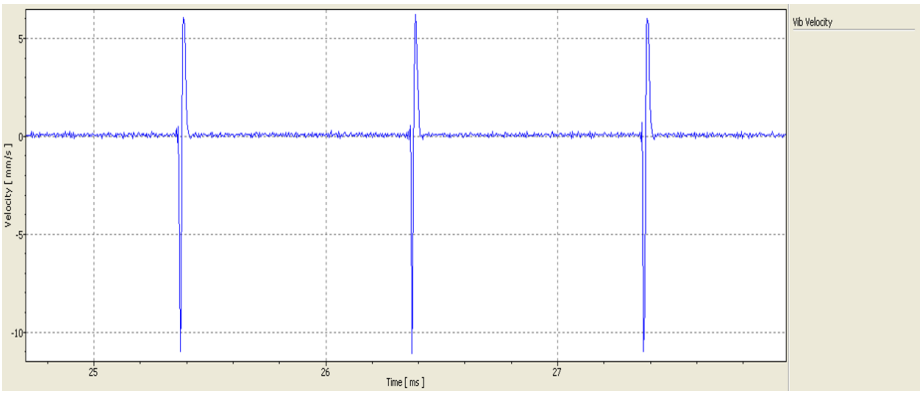

Figure 2.9: A screen capture of the laser vibrometer interface showing the time response of the sensor under a pulse train

2.5 Experimental Limitations

2.5.1 Static charge shock

Static charges are generated from contact between two surfaces, such as fabrics. All materials are made of atoms and electrons; thus, electrons can move from one material to another upon contact. Low humidity helps to accumulate static charges [59]. The human body is a good insulator (highly resistive) as a result, it accumulates static charges. Thus, if an operator wears fabric material and/or rubber shoes static charges tend to accumulate on his/her body. Upon touching a chip, the static charges are released into the specimen through electrical connections resulting in charge shock and stiction either in line-contact or area-contact. Operators were instructed to wear Electrical Discharge Strips (EDS) connected to the common ground of vibrometer to protect the specimen from static charges.

2.5.2 Dielectric charging

Electrostatic charging poses a serious impediment to experimental measurements. It occurs due to buildup of static charges on dielectric layers in a MEMS, which turns them into voltage sources within the MEMS. Specifically, charge buildup on a dielectric layer within the actuation capacitor with the same polarity as the excitation voltage will reduce the effective voltage drop across the capacitor. This is particularly exacerbated by the sense-plate coming into contact with the bottom electrode during pull-in.

In our experiments, we observed that pull-in voltage increased after repeated pull-in cycles. To rule out the formation of debris on top of the bottom electrode (due to impact during pull-in) as a source of this phenomenon, three sensors were broken to able to investigate the bottom electrode by obtaining SEM pictures in three cases:

i) after seven pull-in cycles, Fig. 2.10(a),

ii) after three pull-in cycles, Fig. 2.10(b), and

iii) for a fresh (never pulled-in) sensor, Fig. 2.10(c).

Examining the pictures in Fig. 2.10, we found no debris on the bottom electrode in all three cases, thereby ruling out debris formation as a source of drift in pull-in voltage.

We postulate that increase in pull-in voltage after repeated pull-in cycles occurs due to the formation of a native oxide layer on the bottom polysilicon electrode due to extended exposure to air. Literature shows that extended exposure of bare polysilicon surfaces to air leads typically to the formation of $1-3$ nm thick native oxide layers [60, 61]. However, devices fabricated using PolyMUMPs have been shown to possess an extremely thick, up to 30 nm, native oxide layer [62]. This layer of silicon dioxide serves as a dielectric layer that

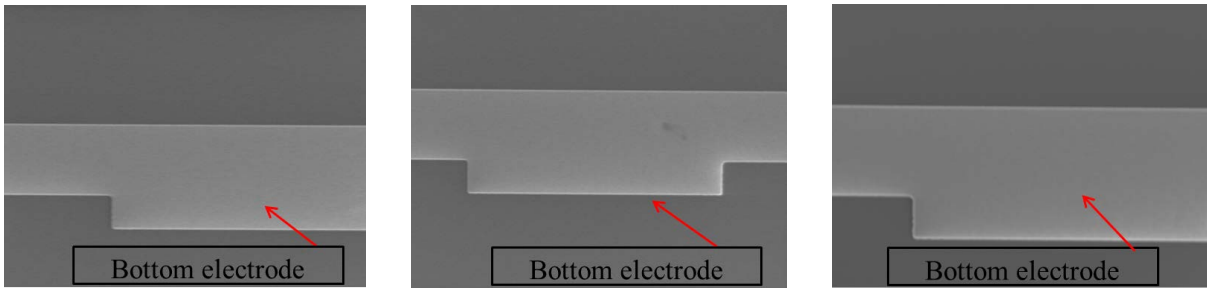

(a) (b) (c)

Figure 2.10: SEM pictures of the bottom electrode for sensors: (a) after seven pull-in cycles, (b) after three pull-in cycles, and (c) no pull-in

contributes to contact resistance and leads buildup of trapped charges, thus modifying the pull-in voltage [63, 64]. The maximum observed increase in pull-voltage was ~ 100 mV.

2.5.3 Contact resistance

Once the electrostatic actuator goes into pull-in, the sense-plate and bottom electrode are transformed from a capacitor into a resistor resulting in a drastic drop in voltage across the plate and bottom electrode. We found that the sense-plate came into contact with the bottom electrode following pull-in in one of two sates: over an area (area-contact) or along a line (line-contact). An LCR meter, Agilent Technologies Inc. U1700 [65], was used to measure contact resistance, impedance, and phase difference between current and voltage across the 'capacitor' under both conditions.

Area-contact

Area-contact occurs when the whole sense-plate collapse onto the bottom electrode transforming the capacitor into a resistor with current draining across the contact area. Sev-

eral experiments were conducted to characterize area-contact, measure resistance and impedance across the junction, and the results are listed in Table. 2.3. The results show that typical resistance and impedance in area-contact is on the order of kΩ. The small difference between the values of resistance and impedance indicate that capacitive loading across the junction is minimal.

Table 2.3: Measured resistance and impedance for two sensors in area-contact

Sensor Index	Resistance (kΩ)	Impedance (kΩ)
A.3	4.35	4.41
A.4	3.97	4.41

Area-contact can also be characterized optically using a CCD camera. Comparison of the cantilever beams before and after pull-in, Figure 2.11, shows fringe fields (lines) appear along the beams following pull-in due destructive light interference over the slopped beam profile. On the other hand, no fringe fields are observed on the sense-plate when it lies level over the bottom electrode in area-contact following pull-in.

Line-contact

Line-contact occurs when the sense-plate is partially pulled-in to come into contact with the substrate along a line. We found that this condition introduces a large resistance between the sense-plate and bottom electrode due to the small contact area. The measured resistance and impedance for three sensors that pulled-in along a line are tabulated in Table. 2.4. In all cases, the LCR meter measured a contact resistance larger than its maximum measurement range, $R_1 > 200$ MΩ.

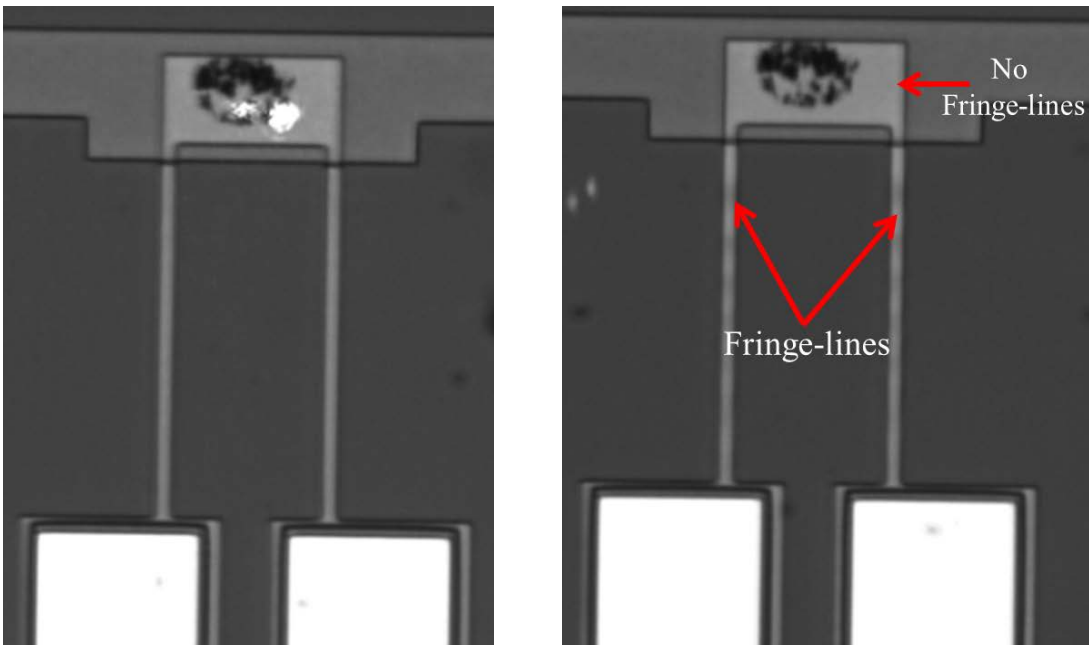

(a) (b)

Figure 2.11: Pictures of (a) the unactuated sensor (0 V) and (b) the sensor in area-contact subsequent to pull-in

On the other hand, the magnitude of the overall impedance across the microplate and bottom electrode Z_t was found to be at least one order-of-magnitude less than contact resistance. This is due to the continued presence of a capacitor connected in parallel with the resistance between the microplate and the substrate, Fig. 2.12. As a result, the overall impedance across the microplate-substrate junction can be written as

$$\begin{aligned} Z_t &= \frac{-R_1 \frac{i}{\Omega C_1}}{R_1 - \frac{i}{\Omega C_1}} \\ &\approx \lim_{R_1 \to \infty} \frac{-R_1 \frac{i}{\Omega C_1}}{R_1 - \frac{i}{\Omega C_1}} = -\frac{i}{\Omega C_1} \end{aligned} \tag{2.23}$$

Table 2.4: Measured resistance and impedance for three sensors in line-contact

Sensor Index	Resistance (MΩ)	Impedance (MΩ)
A.3	> 200	15.4
A.4	> 200	17.0
C.4	> 200	17.7

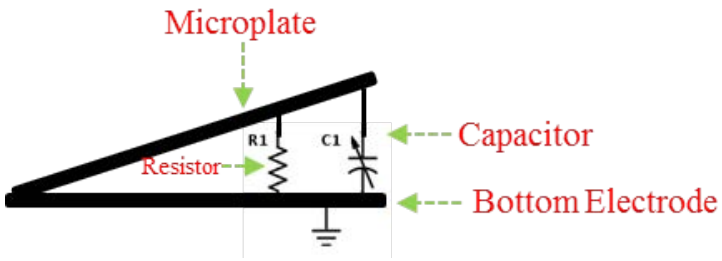

Figure 2.12: Electrical components of line-contact phenomena

Line-contact can also be observed optically using a CCD camera as shown Fig. 2.13. In this case, fringe lines form on the cantilever beams and the sense-plate as a result of the sense-plate lying at an angle with respect to the substrate (slopping towards it).

Capacitor phase shift

There is no phase difference between current and voltage across a resistor. Current leads voltage across a capacitor by a phase angle of 90°. This suggests that a potential technique to detect pull-in electrically is to measure the phase difference between current and voltage across the microplate-bottom electrode junction. We used the LCR meter to measure the phase lead of current with respect to voltage for three sensors, Table. 2.5.

The phase difference for two sensors detected optically to be in line-contact with the

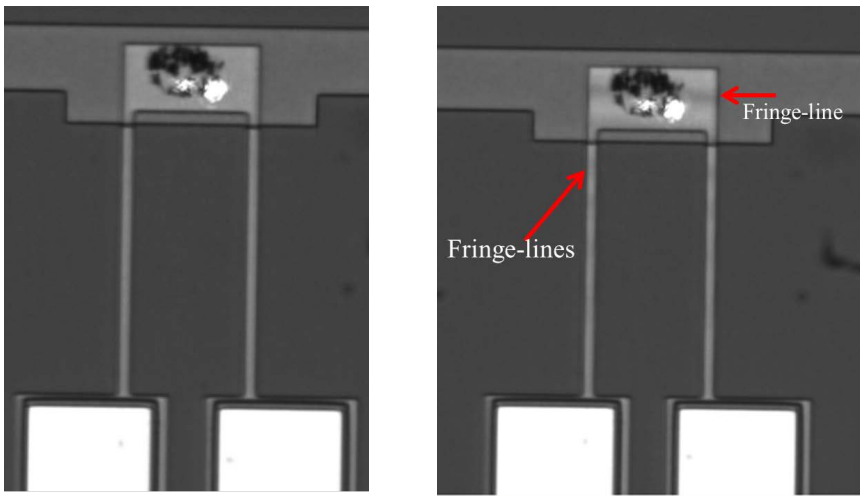

(a) (b)

Figure 2.13: Pictures of (a) the unactuated sensor and (b) the sensor in line-contact subsequent to pull-in

substrate, sensors A.3 and A.4, was close to zero indicating current passage through a resistive load. The phase difference for a sensor detected optically to be in-flight, sensor C.6 ,was 90° indicating the absence of resistive load (sensor in-flight). Therefore, measurement of phase difference between voltage and current across the electrostatic capacitor can be used as a contact detector.

The presence of a thick dielectric layer over the bottom electrode can undermine this detection method. Specifically, we measured the resistance, impedance, and phase difference for a sensor after pull-in as listed in Table. 2.6. While the measured phase shift 89.4° imply no contact, optical inspection showed that the sensor was in area-contact. We postulate that the dielectric layer within the pulled-in capacitor was thick enough to provide contact resistance significantly larger than the capacitor reactance ($R_1 \rightarrow \infty$). As a result, the impedance was dominated by the capacitor reactance and the phase shift stayed to 90°

Table 2.5: Measured impedance and phase shift between microplate and bottom electrode doe three sensors

Sensor Index	Impedance (MΩ)	Phase shift (°)	Status
A.3	15.4	0.2	Line-contact
A.4	17.0	0.6	Line-contact
C.6	17.7	90	No contact

Table 2.6: Measured resistance, impedance, and phase shift for a sensor pulled-in in area-contact

Resistance (kΩ)	Impedance (MΩ)	phase shift (°)	Status
> 200	6.684	89.4	Area contact

after pull-in. This scenario undermines the usability of phase shift as a contact detector.

2.5.4 Limitation of the detection circuit

The detection circuit, Fig. 2.14, described in section 2.1.5 measures the voltage drop across the electrostatic capacitor. An LED turns on when the voltage across the electrostatic capacitor drops below a threshold value due to charge draining to the ground after pull-in. This mechanism malfunctions when the voltage across the capacitor drops slowly after pull-in due to high overall impedance Z_t.

A test was conducted on the detection circuit to simulate contact-resistance during pull-in and determine the maximum allowable shunt resistance. The detection circuit was loaded with a 1 GΩ resistor connected in parallel to a 100 pF ceramic capacitor, representing the

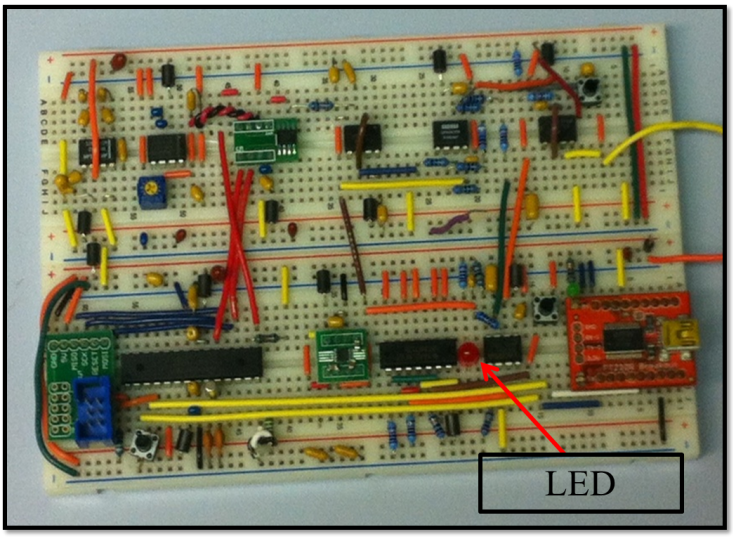

Figure 2.14: The gas sensor drive/detection circuit

sensor capacitance. The circuit required 4 minutes to discharge the capacitor and turn on the LED. On the other hand, the detection circuit required longer time to detect contact after each pull-in, ranging from a minimum of a few seconds, for a fresh sensor, up to tens of minutes after seven pull-in cycles. The experiment indicates that pull-in cycles increases contact resistance drastically.

2.6 Experimental setup

The experimental setup, Fig. 2.15, is composed of the sensor inside a test chamber, the drive and detection circuit, and gas canister containing a pre-calibrated test gas charge. It insures dual electrical and optical observation of the sensor, thus testing and verifying the performance of the sensor and drive and detection circuit. A test chamber shown in Fig. 2.16, volume 160 cm^3, was designed to control the composition of the gas mixture to which the sensor is exposed. The chamber is equipped with an electrical interface, BNC

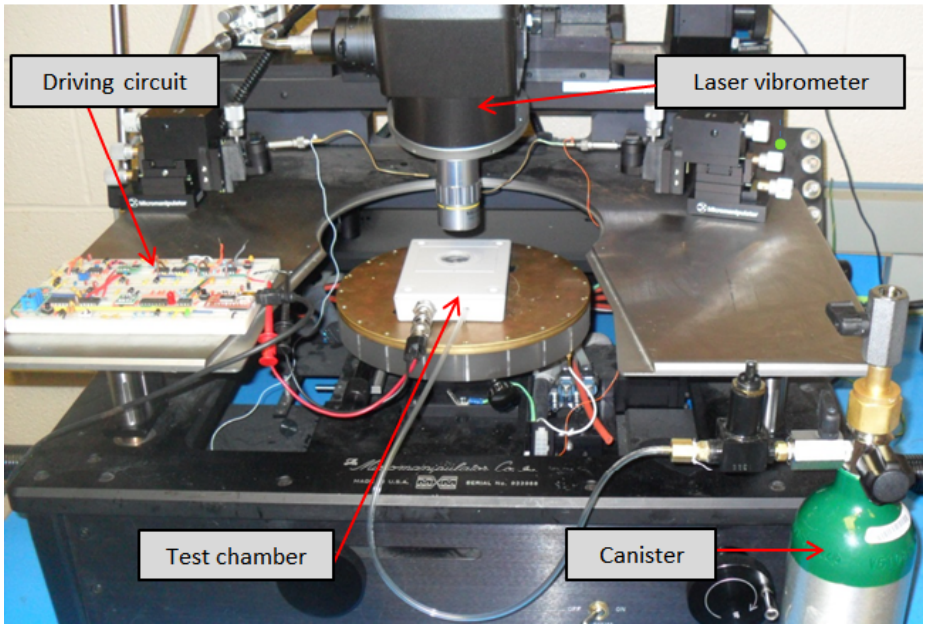

Figure 2.15: The experimental setup

port, to connect the sensor to the drive and detection circuit, and a quartz glass window to allow for optical detection and measurement of the sensor response using a vibrometer. The gas canister is used to release a pre-calibrated mixture of dry nitrogen and ethanol into the test chamber by opening the canister valve to allow the gas to flow under its own pressure into the chamber.

Experiments are conducted by placing the sensor inside the test chamber and commanding the drive circuit using a PC to apply the operating voltage $V_\circ$ to the sensor while in ambient air. The canister valve is then fully opened and the gas mixture is allowed to flow for three minutes into the test chamber to purge out air. Subsequently, gas flow is reduced slowly to a minimum to protect against the possibility of gas flow sending the sensor into a false detection. The sensor response is monitored continuously using a video CCD camera to detect fringe fields and the LED in the drive and detection circuit.

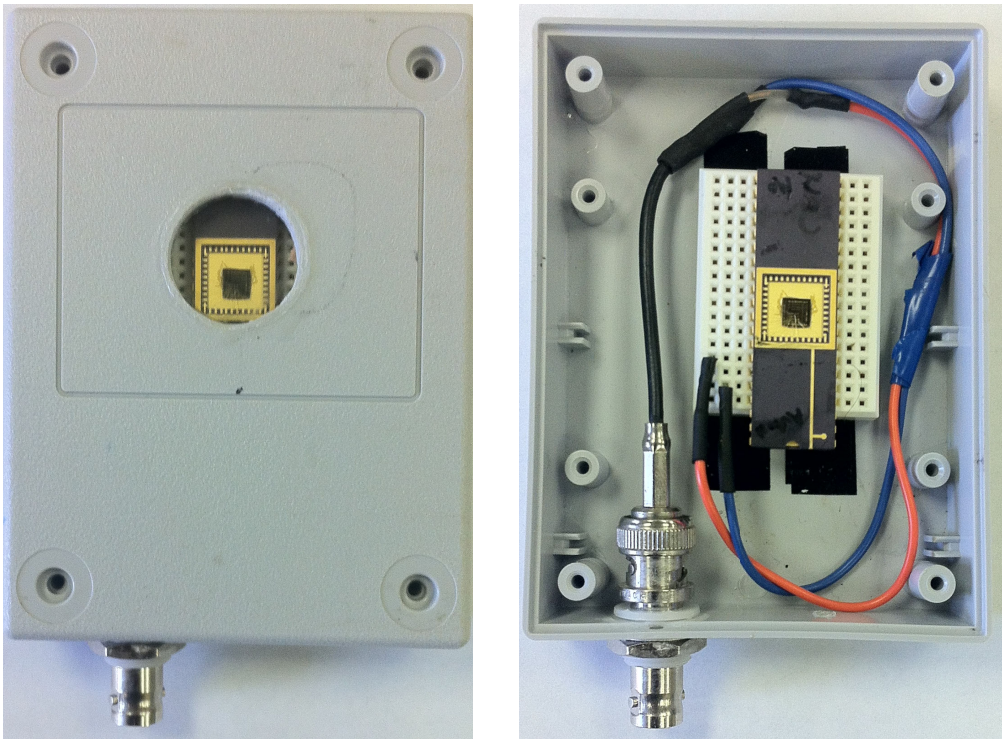

(a) (b)

Figure 2.16: The test chamber is equipped with (a) quartz glass window and (b) a BNC port

2.7 Results

A series of experiments were conducted to determine the minimum detectable ethanol concentration (detection limit) for sensors equipped with PANI-10% NiO and P25DMA. The test gases were made of ethanol vapor in dry nitrogen at concentrations ranging from 1000 ppm to 5 ppm.

2.7.1 Ethanol detection using PANI-10% NiO

To test the detection limit of the sensor equipped with PANI polymer, it was placed inside the test chamber. The test gases had ethanol vapor concentrations of 1000, 100, and 50 ppm. We define the set-off voltage as the difference between the pull-in voltage $V_{\rm pi}$ and the operating voltage $V_\circ$:

$$\delta V = V_{\rm pi} - V_\circ$$

The following experiments were conducted:

1000 ppm ethanol vapor in dry nitrogen: The set-off voltage was set to $\delta V = 20$ mV. After 195 seconds, pull-in was observed to occur optically in area-contact, Fig. 2.17(a), and electrically by turning the LED ON.

100 ppm ethanol vapor in dry nitrogen: The set-off voltage was set to $\delta V = 15$ mV. After 120 seconds, pull-in was observed optically to occur in line-contact, Fig. 2.17(b). Since impedance of the pulled-in microplate was high, the LED turning on was significantly delayed, several minutes, by beyond pull-in.

50 ppm ethanol vapor in dry nitrogen: The set-off voltage was set to $\delta V = 1$ mV. After 80 seconds, pull-in was observed optically to occur in line-contact. The results of the experiments are summarized in Table 2.7. Since the actuation circuit resolution is 1 mV, no further experiments were conducted.

The black spot appearing on the sense-plate in Fig. 2.17 is the PANI deposited on the sense-plate. The fringe lines observed on the cantilever beams only in Fig. 2.17(a) indicate area-contact, while The fringe lines observed on the sense-plate and cantilever beams in Fig. 2.17(b) indicate line-contact. We conclude that the added mass in the 100 pm and 50 ppm ethanol vapor was less than that in the 1000 ppm ethanol vapor leading to line instead of area-contact.

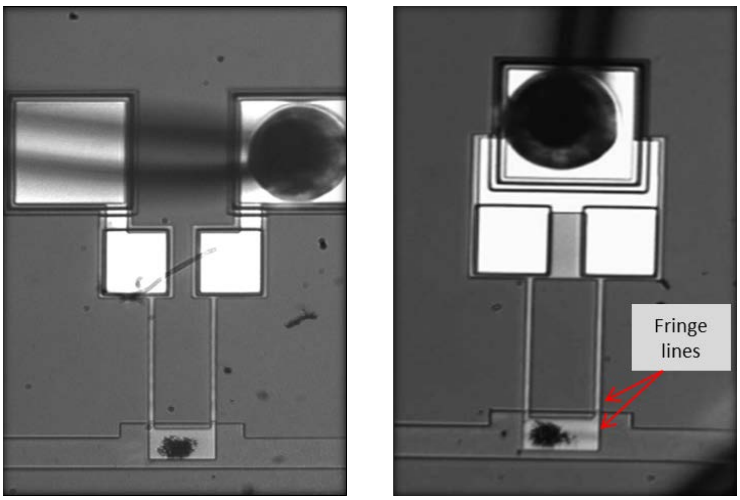

(a) (b)

Figure 2.17: PANI-equipped sensor (a) in area-contact after detection of 1000 ppm ethanol in dry nitrogen and (b) in line-contact after detection of 100 ppm ethanol in dry nitrogen

To estimate the added mass listed in Table. 2.7, we used the operating voltage $V_\circ$ to determine the sensor sensitivity S_m from Fig. 2.5, and the displacement due to add mass

$$\delta w = w_\mathrm{pi} - w_c$$

from Fig. 2.4. The added mass was then calculated as their ratio

$$\delta m = \frac{\delta w}{S_\mathrm{m}}$$

2.7.2 Ethanol detection using P25DMA

The P25DMA-equipped sensor was tested using gas mixtures with ethanol concentrations of 50 and 5 ppm. The initial set off voltage was $\delta V = 20$ mV.

Table 2.7: Experimental results for the PANI-equipped binary ethanol sensor (EtOH)

Set-off Voltage (mV)	EtOH Concentration (ppm)	Estimated Mass δm (pg)	Response Time (s)
20	1000	845	195
15	100	727	120
1	50	165	80

The following experiments were conducted:

50 ppm ethanol vapor in dry nitrogen: the operating voltage, $V_\circ$, was increased in steps of 1 mV with a hold-off period of 600 s after each step. The hold-off period is eight orders of magnitude higher than the settling time, $t_s = 20$ μs, guaranteeing elimination of transient effects. Pull-in occurred at a set-off voltage of $\delta V = 5$ mV after 45 seconds. It was observed to occur optically in line-contact.

5 ppm ethanol vapor in dry nitrogen: the operating voltage, $V_\circ$, was increased in steps of 1 mV with a hold-off period of 30 s after each step. The hold-off period is six orders of magnitude higher than the settling time, $t_s = 20$ μs, guaranteeing elimination of transient effects. Pull-in occurred at a set-off voltage of $\delta V = 1$ mV after 7 seconds. It was observed optically to occur in line-contact.

The results of the experiments are summarized in Table 2.8. Since the actuation circuit resolution is 1 mV, no further experiments were conducted. We note that all the experimental results were repeated at least twice to ensure repeatability of detection.

Table 2.8: Experimental results for the P25DMA-equipped binary ethanol sensor (EtOH)

Set-off Voltage (mV)	EtOH Concentration (ppm)	Estimated Mass δm (pg)	Response Time (s)
5	50	407	45
1	5	165	7.0

2.8 Discussion

The detection limit of the ethanol sensor equipped with PANI doped with 10% NiO was 50 ppm, whereas the detection limit for the sensor equipped with P25DMA was 5 ppm. It is important to note that the minimum detectable concentration is dependent on the minimum realizable set-off voltage δV and the type, amount, and distribution of the detector polymer coating the sense-plate. Since the same procedure was used in preparing, depositing, and testing the two detector polymers, our results show that the sensitivity of P25DMA to ethanol vapor is one order-of-magnitude more than that of PANI doped with 10% NiO.

The minimum detectable mass was 165 pico-grams at a set-off voltage $\delta V = 1$ mV. The fact that we could realize a level of mass sensitivity competitive with more elaborate MEMS mass sensors using fringe field detection only shows the potential advantages of bifurcation-based sensing. Further, we note that all experiments were conducted in air on a probe station that was not isolated from ground vibration. Further, no precautions were taken to protect the sensors against external disturbances. However, there was no false positives reported in any of the series of experiments conducted with this sensor. This observation indicates that the stability of MEMS inertial sensors against external

disturbances is better than macro sized sensors because of the minute mass of the sense-plate, on the order of a few nano-grams. The fact that our sensor is over-damped added another layer of protection against external disturbances.

Chapter 3

Magnetic Sensor

This chapter presents a novel MEMS magnetic sensor based on the Lorentz force. Most magnetic sensors available commercially have a narrow dynamic measurement range. The proposed magnetic sensor seeks to achieve a small size, a wide adjustable dynamic range, and a programmable sensitivity. It utilizes a Lorentz force, generated by an alternating current and an external magnetic field, to excite a torsional mode. This sensor has multiple operating points that determine its sensitivity and dynamic range. Modal analysis is carried out for the sensor and experiments are conducted to verify for the torsional mode and other modes in its vicinity.

3.1 Principle of Operation

The magnetic sensor, Fig. 3.1, is based on the same structure used for the binary gas sensor presented in chapter 2. Its torsional mode is excited by two signals V_a and V_b applied to the bonding pads of the cantilever beams. A phase difference of 180° is maintained between

the two signals as follows

$$V_a = V_{dc} + V_{p1}\sin(2\pi f_\circ t) \tag{3.1}$$

$$V_b = V_{dc} + V_{p2}\sin(2\pi f_\circ t + \phi) \tag{3.2}$$

where $f_\circ$ is the signal frequency. Because of the symmetry in the released sensor structure, the voltage drop from one pad to the microplate is identical to that from other pad to the microplate. When the amplitudes of V_a and V_b are set to $V_{p1} = V_{p2}$ and the phase difference between them is set to $\phi = \pi$, the voltage drop between the microplate and the bottom (ground) electrode is equal to the DC bias V_{dc} of the excitation signals.

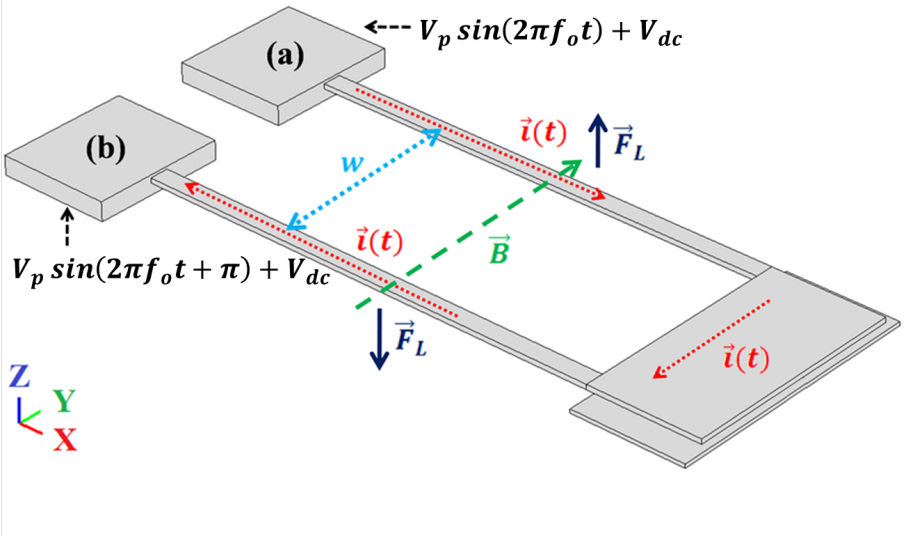

Figure 3.1: Isometric view of the magnetic sensor showing the excitation current (red dotted lines), the external magnetic field (green dashed line), and the Lorentz force (blue solid lines)

An electrostatic force develops, due to the bias voltage V_{dc}, between the microplate and the bottom electrode. It moves the microplate downward to settle at a point in the electrostatic field corresponding to the applied force.

The excitation current $\vec{i}(t)$ passing through the two cantilevers beams interacts with the external magnetic field $\vec{B}(t)$ to induce a force $\vec{F_L}$ orthogonal to the current and magnetic field, Fig. 3.1, as per Lorentz Law [66],

$$\vec{F_L} = l_c \vec{i}(t) \times \vec{B} \tag{3.3}$$

where l_c is the length of the cantilever beam, Fig. 3.2,. The Lorentz force-pair acting on the two beams are equal in magnitude, due to symmetry, and opposite in directions. The force pair creates an excitation torque acting on the microplate

$$T_m = w l_c i(t) B \tag{3.4}$$

where w is the distance between the center lines of the micro-beams. It drives microplate into torsional oscillations at the common frequency of the actuation signals $f_\circ$. Slow variations in the magnetic field strength $\vec{B}(t)$ over time modulate the amplitude of torsional oscillation. As a result, the external magnetic field acts as a baseband signal modulating the torsional oscillations of the microplate where the excitation current acts as a carrier signal.

The linear relationship between the magnetic field $\vec{B}$ and Lorentz force, Eq. (3.3), allow for a linear relationship between the magnetic field $\vec{B}$ and the measured; the microplate oscillations. All three spatial components of the magnetic field can be measured using three identical magnetic sensors placed along the axes of an orthogonal coordinate system. The reversal of the magnetic field direction along an axis can be detected as a phase shift of 180° in the phase angle between the microplate oscillations and the excitation signals.

The bending-torsional motions of the sensor can be described using a lumped-mass model as a set of two second-order ordinary differential equations describing the microplate

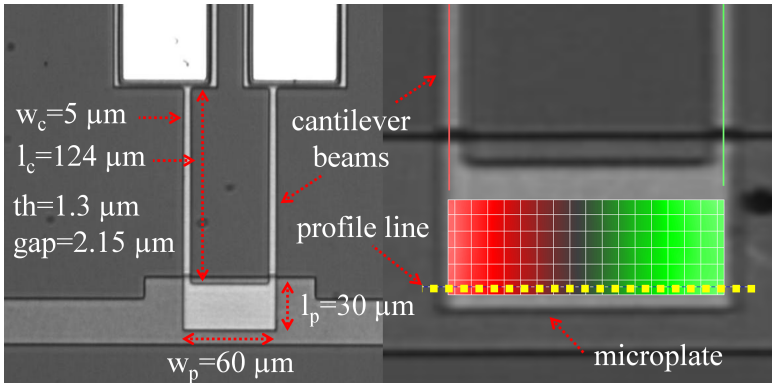

Figure 3.2: Top view (left) of the magnetic sensor and the microplate (right) color coded with measured displacement (red: high; green: low) when excited into torsional oscillations

vertical z and angular θ displacements [46, 67]:

$$m\ddot{z} + c_b\dot{z} + k_b z = \frac{1}{2}\frac{\epsilon w_p l_p V_{dc}^2}{(d-z)}\left(\frac{1}{2d-2z-l_p\theta} + \frac{1}{2d-2z+l_p\theta}\right) \tag{3.5}$$

$$J\ddot{\theta} + c_t\dot{\theta} + k_t\theta = w l_c i(t) B + T_e \tag{3.6}$$

where m is the effective mass of the sensor, J is the second moment of inertia of the microplate around its center line, k_b and k_t are the effective bending and torsional stiffness of the beams, and c_b and c_t are bending and torsional viscous damping coefficients combining the energy losses due to structural, squeeze-film, and other damping sources. The microplate length and width are denoted l_p and w_p, respectively, and the gap distance between microplate and bottom electrode is donated d. The torque due to electrostatic forces T_e is described by:

$$T_e = -\epsilon_0 V^2 \frac{sin^2\theta}{2\theta^2}\int_0^{l_p}\int_{-\frac{1}{2}w_p}^{\frac{1}{2}w_p}\left(\frac{1}{d-ysin\theta}\right)^2 ydydx \tag{3.7}$$

The magnitude of the electrostatic force, Fe, and electrostatic torque, T_e, are proportional to the square of the voltage drop between the microplate and bottom electrode V, which

is not necessarily equal to V_{dc}. The harmonic components of the electrostatic force and torque can be derived by squaring a generic waveform $V = V_{dc} + V_p \sin(2\pi f_\circ t)$ as:

$$\begin{aligned} V(t)^2 &= (V_{dc}^2 + \tfrac{1}{2}V_p^2) + 2V_{dc}V_p \sin(2\pi f_\circ t) - \tfrac{1}{2}V_p^2 \cos(4\pi f_\circ t) \\ &\propto Fe_{dc} + Fe_1 + Fe_2 \\ &\propto Te_{dc} + Te_1 + Te_2 \end{aligned} \tag{3.8}$$

where Fe_{dc} and Te_{dc} are the static component, Fe_1 and Te_1 are the first harmonic component, and Fe_2 and Te_2 are the second harmonic component. Eqs. (3.5) and (3.6) represent a lumped model, Fig 3.3, for bending motions, due to electrostatic forces used to adjust the sensor sensitivity, and torsional motions, due to electrostatic and electromagnetic torques.

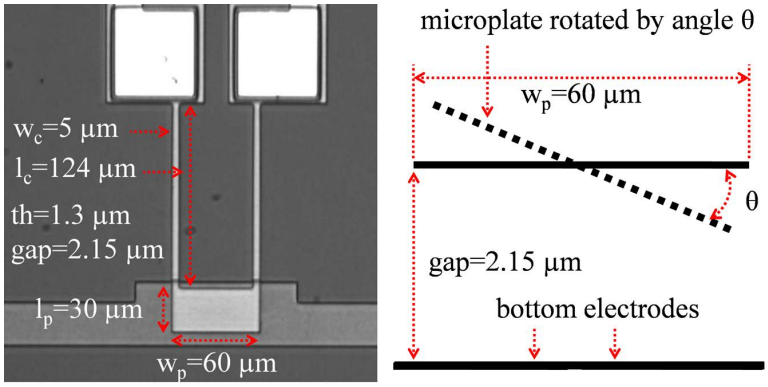

Figure 3.3: (a) Top and (a) front views of the magnetic sensor

For bias voltages V_{dc}, Eq. (3.5), larger than zero, electrostatic forces will develop between the microplate and the bottom electrode. As a result, the microplate will move downward to settle at a point closer to the bottom electrode, thereby increasing the electrostatic field strength at the equilibrium point. Therefore, the magnitude of the bias voltage can be used to set the operating point and sensitivity of the magnetic sensor. This adjusts the sensitivity and dynamic range of the sensor in the following ways:

– It decreases the natural frequency and stiffness of the sensor torsional motions resulting in larger sensor motions in response to the same level of Lornetz force (magnetic field strength).

– A smaller capacitor gap increases the sensitivity of capacitive sensing for the same size sensor motions.

– A smaller capacitor gap increases squeeze-film damping which decreases the size of sensor motions in response to the same level of Lornetz force.

We note that the relationship between bias voltage (operating point) and sensitivity is not linear or monotonic and, therefore, requires an optimization process to identify a set of optimal operating points.

3.2 Numerical Model

A finite element model (FEM) of the magnetic sensor was created in COMSOL to calculate its natural frequencies and mode shapes. The model was made of 4650 hexahedral elements. It did not account for the electrostatic field or fluid-structure interactions. Fig. 3.4 shows the first four mode shapes and natural frequencies of the magnetic sensor obtained from eigenvalue analysis in COMSOL.

The first mode shape is the first out-of-plane bending, Fig. 3.4(a), with a natural frequency of $f_1 = 34$ kHz. The second mode shape is the first torsional mode, Fig. 3.4(b), with a natural frequency of $f_2 = 198$ kHz. The third mode shape is the first in-plane bending, Fig. 3.4(c), with a natural frequency of $f_3 = 283$ kHz. The fourth mode shape is the second out-of-plane bending, Fig. 3.4(d), with a natural frequency of $f_4 = 368$ kHz.

The widely spaced modes reduce the possibility of modal interaction between the sensing mode, the first torsional mode, and other modes of sensor vibrations.

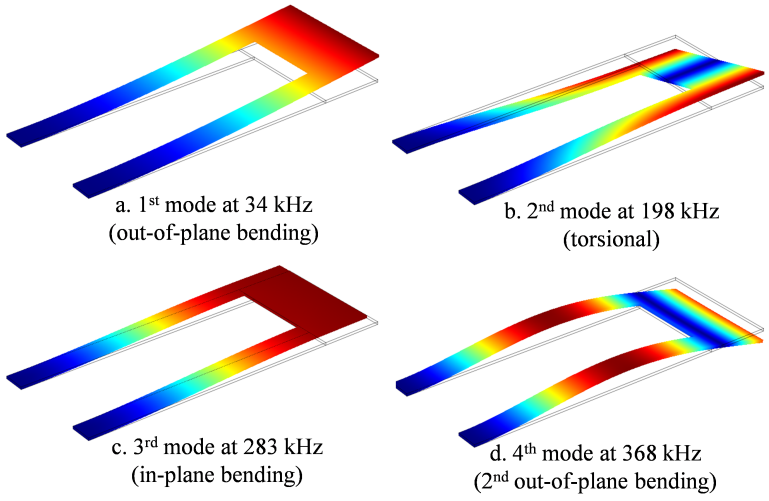

Figure 3.4: The first four undamped mode shapes of the magnetic sensor obtained from eigenfrequency analysis using COMSOL

3.3 Experimental Results

The natural frequencies and mode shapes of the first two modes were determined experimentally by direct non-contact measurements of the sensor response using a laser vibrometer, Polytec MSV400, and the experimental setup is shown in Fig. 3.5. Velocity decoder VD-02 and displacement decoder DD-300 were used to measure the microplate velocity and displacement, respectively. The measured resistance between bonding pads (a) and (b), in Fig. 3.1, was found to be $R_c = 1.517$ kΩ.

A constant magnetic field was applied to the sensor throughout measurements of the sensor response. The amplitude of the excitation signals V_a and V_b was set to $V_{p1} = V_{p2} =$

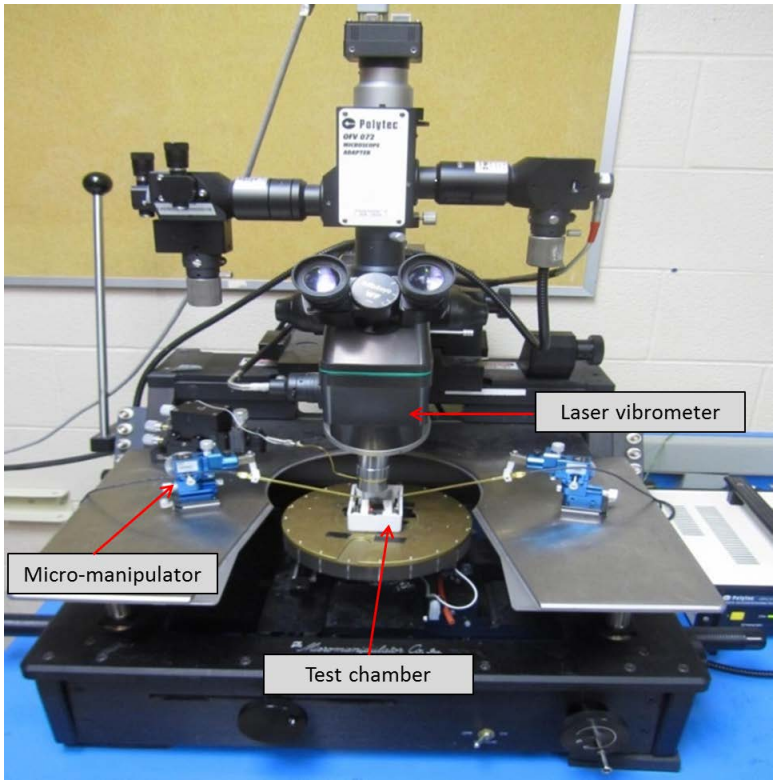

Figure 3.5: Experimental set-up showing the laser vibrometer, probe station, micro manipulators, and specimen

5 V throughout the experiments, while the excitation frequency was varied until maximum response was obtained at resonance f_i. The amplitude in the current loop was calculated by Ohm's law

$$I_c = \frac{V_p}{R_c} \tag{3.9}$$

to be $I_c = 6.6$ mA.

3.3.1 Modal response

We measured the natural frequencies and mode shapes of the first bending mode and first torsional mode. A function generator supplied the excitation signals V_a and V_b to the bonding pads and a manual frequency sweep was carried out in the frequency range $[0, 400]$ kHz to locate the natural frequencies. Velocity was measured at the microplate center, point A in Fig. 3.6, for the bending mode and at the microplate edge, point B, for the torsional mode.

A line-grid made of 42 points on each of the cantilever beams and an area-grid made of 133 points on the microplate were defined on the sensor strucure, Fig. 3.6. The "multi-scan" feature of the vibrometer was used to measure the response of the sensor at each grid point, when the sensor was excited at a natural frequency. The measurements were used in the PSV software to obtain the mode shape corresponding to that natural frequency.

Bending mode

To excite bending oscillations, the phase angle between the excitation signals V_a and V_b was set to $\phi = 0°$ and the bias voltage to $V_{dc} = 0$. This excitation regime resulted in the application of a downward electrostatic force on the microplate but did not induce current in the loop and, therefore or electromagnetic torque. The electrostatic force was made of the Fe_2 component, Eq. (3.8), only. As a result, the dominant excitation frequency was twice the signals frequency $2f_\circ$. Table 3.1 lists the measured velocity amplitude of point A at the signal frequency $f_\circ$ and the excitation frequency $2f_\circ$ for three selected cases, $f_\circ = 7.5$, 15.5, and 31 kHz, within a frequency sweep in the range $f_\circ = [0, 100]$ kHz.

The the natural frequency of the first out-of-plane bending mode was found at an excitation frequency of $2f_\circ = 31$ kHz where the measured velocity amplitude of bending

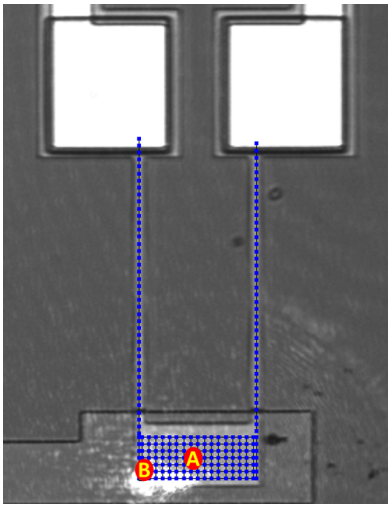

Figure 3.6: Two measured points, A and B, for the bending and torsional modes

Table 3.1: Bending mode excitation signals and their response

Case	V_{p1} (V)	V_{p2} (V)	$f_\circ$ (kHz)	$v(f_\circ)$ (mm/s)	$v(2f_\circ)$ (mm/s)
1	5	5	7.5	0.241	5.00
2	5	5	15.5	0.182	5.93
3	5	5	31	0.317	4.96

motions reached a maximum of $v(2f_\circ) = 5.93$ mm/s. The first harmonic response appearing at $f_\circ$ is due to an of amplification of DC noise by the AC signals V_{pi} resulting in an electrostatic force component F_{e1}. The difference between the measured natural frequency and that found by FEM in section 2.4.3 is due to inter-chip and intra-chip dimensional variability as well as variation in material properties between the two PolyMUMPs runs used to fabricate the sensors.

The first out-of-plane bending mode shape obtained from a multi-scan experiment with an excitation frequency of $2f_\circ = 31$ kHz is shown in Fig. 3.7. The figure shows the sensor strucure at a terminal position in the cycle of oscillations color coded with red representing

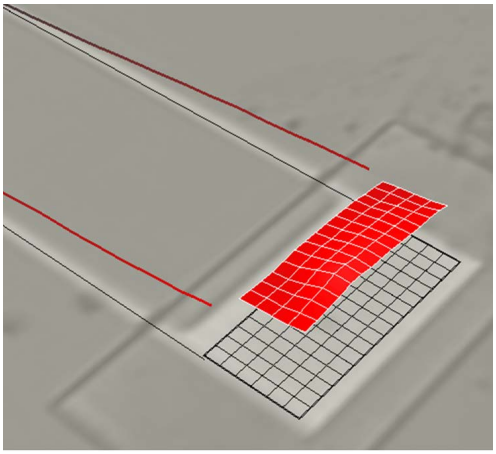

Figure 3.7: The mode shape of the first out-of-plane bending mode obtained experimentally at $2f_\circ = 31$ kHz

maximum displacement. Comparison of the experimentally obtained mode shape to that obtained using FEM, Fig. 3.8, shows close agreement. The drop in the measured natural frequency compared to that calculated using FEM is due to the absence of damping in the FEM model. The effect of damping will be addressed in section 3.4.

Torsional mode

The phase angle between the excitation signals V_a and V_b was set to $\phi = 180°$ and the bias voltage to $V_{dc} = 0$ to excite the torsional mode. This setup is designed to apply electromagnetic torque and no electrostatic forces on the microplate, since it should results no voltage drop across the actuation capacitor. While it induces current in the loop, the application of an electromagnetic torque requires, in addition, the present of an electromagnetic field $B \neq 0$. The velocity amplitude was observed at point B using the vibrometer. The frequency spectrum of the response contained two peaks at the signal frequency $f_\circ$ and its second harmonic $2f_\circ$. No precautions were taken to reduce stray magnetic fields in the test

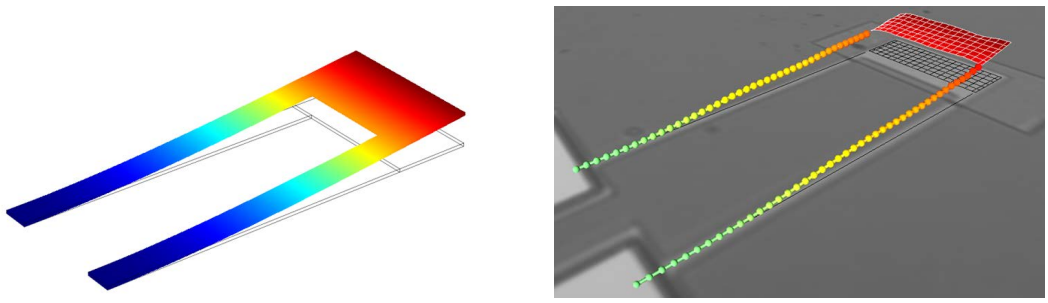

(a) (b)

Figure 3.8: Comparison of the first out-of-plane bending mode shape obtained by (a) FEM at 34 kHz (b) and experimentaly at 31 kHz

environment.

Table 3.2: Torsional mode excitation signals and their response

Case	V_{p1} (V)	V_{p2} (V)	$f_\circ$ (kHz)	ϕ (°)	B (mT)	$v(f_\circ)$ (μm/s)	$v(2f_\circ)$ (μm/s)
1	5	5	31	180	0	22.5	645.5
2	4.5	4	31	180	0	12.8	467.3
5	4.5	4	182	180	27.8	9491.2	28.8

Two experiments were conducted to examine the torsional response of the sensor. The first experiment, comprised of the first two test cases in Table 3.2. Initially, the excitation signals were set amplitudes of $V_{p1} = V_{p2} = 5$ V and a common frequency of $f_\circ = 31$ kHz. The FFT of the measured velocity amplitude at point B contained only two peaks at the signal frequency and its second harmonic. The magnitudes of those peaks were $v(f_\circ) = 22.5$ μm/s and $v(2f_\circ) = 645.5$ μm/s as listed in Case # 1, Table 3.2.

The peak at $f_\circ$ is due to a combination of amplification of DC noise by the AC signals V_{pi} resulting in the electrostatic force component F_{e1}, and an electromagnetic torque caused

by interaction between the current and stray magnetic fields. The peak at $2f_\circ$ is due to residual electrostatic forces caused by the finite width of the microplate and asymmetry in the path resistance on either side, which produce a non-zero voltage drop across the plate. The desired torsional vibrations occur at the signal frequency $f_\circ$ due to electromagnetic torque, Eq.(3.4). In this context, the electrostatically driven bending motions appearing at $f_\circ$ and $2f_\circ$ represent spurious responses.

To reduce those spurious motions, we adjusted the amplitude of the excitation signals to counteract the asymmetry in the path resistance and minimize the residual electrostatic actuation. Minimum response at $f_\circ$ was obtained for, the signal amplitudes of $V_{p1} = 4.5$ V and $V_{p2} = 4$ V where the measured velocity amplitudes were $v(f_\circ) = 12.8$ μm/s and $v(2f_\circ) = 467.20$ μm/s. Reducing the microplate response further, specially at $2f_\circ$, is not feasible given the current design of the microplate, which imposes a significant sheet resistance within the plate, and the presence of stray magnetic fields.

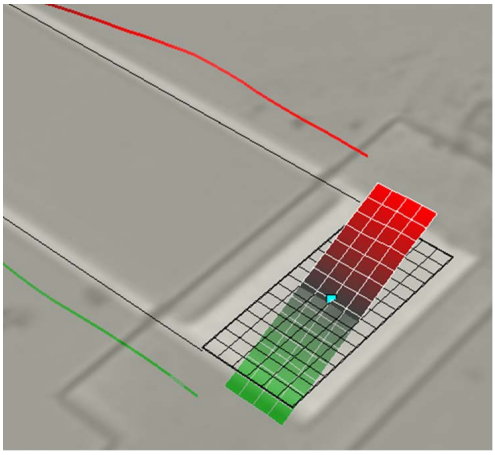

Figure 3.9: The first torsional mode shape obtained experimentally at $f_\circ = 182$ kHz

The second experiment, Case # 3, applied electromagnetic torque to the sensor to investigate its torsional response. A magnetic field $B = 27.8$ mT was applied to the

sensor while it was excited with the optimal signal amplitudes obtained in Case # 2 and a manual frequency sweep was carried out in the frequency range $f_\circ = [0 - 400]$ kHz. The maximum velocity of point B $v(f_\circ) = 9491.2$ μm/s was found at the natural frequency of the first torsional mode $f_\circ = 182$ kHz. For these operating conditions, the spurious motions due to residual electrostatic forces and plate bending at the second harmonic were $v(2f_\circ) = 28.8$ μm/s which is equivalent to a signal-to-noise ratio of $SNR = 22.6$.

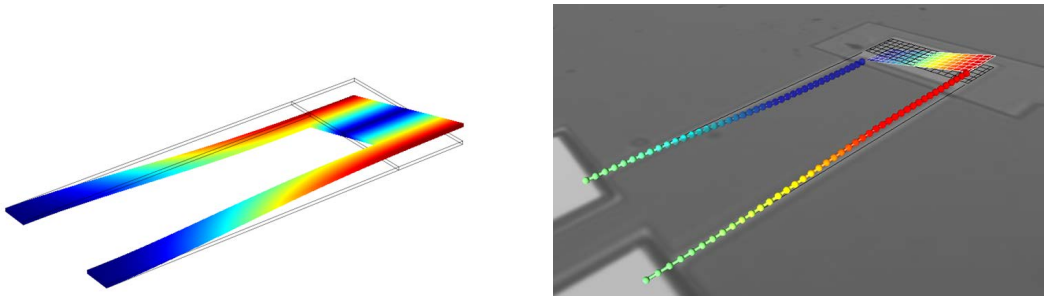

(a) (b)

Figure 3.10: Comparison of the first torsional mode shape obtained by (a) FEM at 198 kHz and (b) experimentally at 182 kHz

The first torsional mode shape, Fig. 3.9, was obtained from a multi-scan experiment with an excitation frequency of $f_\circ = 182$ kHz and a magnetic field strength of $B = 27.8$ mT. The figure shows the sensor strucure at a terminal position in the cycle of oscillations color coded with red representing maximum absolute displacement and green representing minimum absolute displacement. Comparison of the experimentally obtained mode shape to that obtained using FEM, Fig. 3.10, shows close agreement. The drop in the measured natural frequency compared to that calculated using FEM is due to the absence of damping in the FEM model. The effect of damping will be addressed in section 3.4.

3.4 Sensor Demonstration

The sensor can be operated in either forced or resonant modes. Forced mode operation calls for exciting the sensor at a constant frequency faraway from resonance. Resonant mode operation calls for exciting the sensor with a signal frequency in the vicinity of a torsional natural frequency. In this case, we chose to operate the resonant mode at the first torsional natural frequency, $f_\circ = 182$ kHz, to obtain maximum response for a given electromagnetic torque and damping level.

3.4.1 Forced mode

In this section, we compared the sensor response for two test conditions: in the presence and absence of a magnetic field, $B = 27.8$ mT and $B = 0$ mT, respectively, with the same operating conditions as listed in Table 3.3. In both cases, the optimal signal amplitudes were used to excite the sensor at a common frequency of $f_\circ = 31$ kHz and the response velocity was measured at point B. Two peaks in the frequency domain were observed at the signal frequency $f_\circ$ and its second harmonic $2f_\circ$.

Table 3.3: Forced-mode sensing

Case	V_{p1} (V)	V_{p2} (V)	$f_\circ$ (kHz)	ϕ (°)	B (mT)	$v(f_\circ)$ (μm/s)	$v(2f_\circ)$ (μm/s)
1	4.5	4	31	180	0	12.8	467.3
2	4.5	4	31	180	27.8	288.6	444.9

The measured velocity amplitude at the forcing frequency $f_\circ$ increased 23 times, Table 3.3, once an external magnetic field, $B = 27.8$ mT, was introduced. The FFTs of the measured velocity at B in the presence and absence of the magnetic field are shown in Fig. 3.11. In comparison, the change in the response at the second harmonic, caused

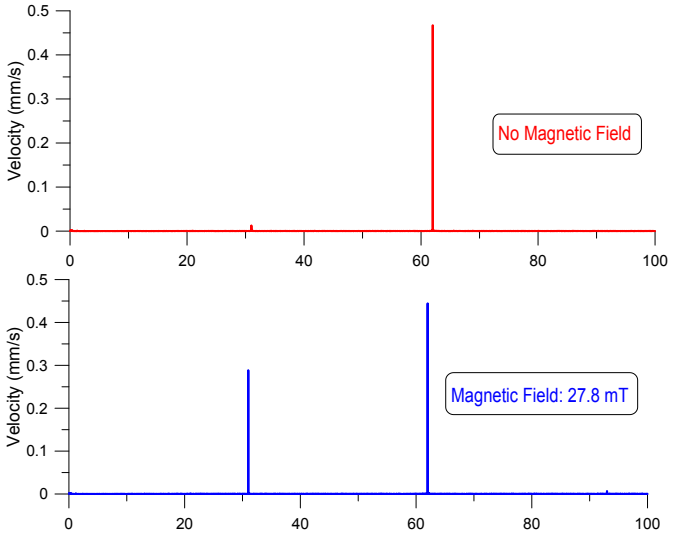

Figure 3.11: The FFTs of the measured velocity amplitude at point B in (a) the absence and (b) presence of an external magnetic field $B = 27.8$ mT when operated in forced-mode $f_\circ = 31$ kHz

by residual electrostatic forces, due to the introduction of the external magnetic field was minimal changing from $v(2f_\circ) = 467.3$ to $v(2f_\circ) = 444.9$ μm/s.

3.4.2 Resonant mode

Table 3.4: Resonant-mode sensing

Case	V_{p1} (V)	V_{p2} (V)	$f_\circ$ (kHz)	ϕ (°)	B (mT)	$v(f_\circ)$ (mm/s)	$v(2f_\circ)$ (μm/s)
4	4.5	4	182	180	0	0.350	13.5
5	4.5	4	182	180	27.8	9.381	28.8

Resonant-mode sensing was employed to increase the magnetic sensor sensitivity and bandwidth. Towards that end, the signal frequency was set equal to the first torsional

natural frequency $f_\circ = 182$ kHz. The same operating conditions were applied to the sensor, Table 3.4, and its response, velocity of point B, was measured in the presence and absence of a magnetic field, $B = 27.8$ mT and $B = 0$ mT, respectively. The velocity amplitude at $f_\circ$ increased 27 times from 0.34 mm/s to 9.38 mm/s once the external magnetic field $B = 27.8$ mT was introduced. The FFTs of the measured velocity at point B in the presence and absence of the magnetic field is shown in Fig. 3.12. The velocity of the response to the residual electrostatic force at $2f_\circ = 364$ kHz was minimal, $v(2f_\circ) = 28$ μm/s, in fact indistinguishable from the noise floor, Fig. 3.12.

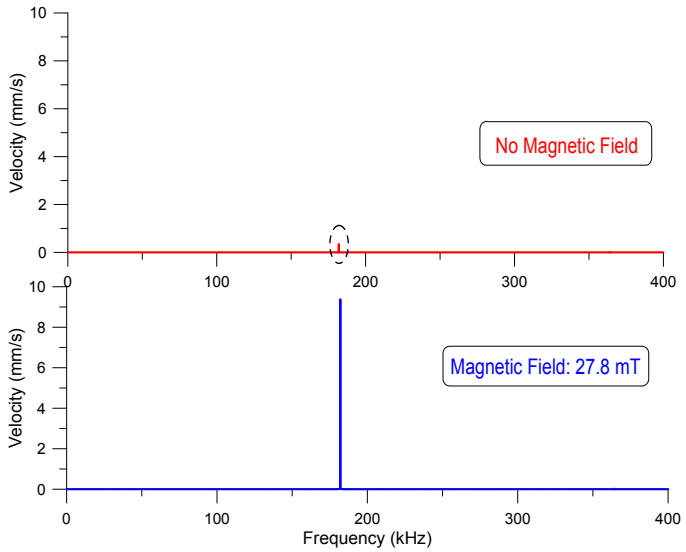

Figure 3.12: The FFTs of the measured velocity amplitude at point B in (a) the absence and (b) presence of an external magnetic field $B = 27.8$ mT when operated in resonant-mode $f_\circ = 182$ kHz

Comparing the results shown in Figs. 3.11 and 3.12, it is evident that the sensor can be operated in either forced or resonant-modes. However, resonant-mode operation increases the sensitivity and the SNR of the sensor from 23 to 27. Specifically, comparison between

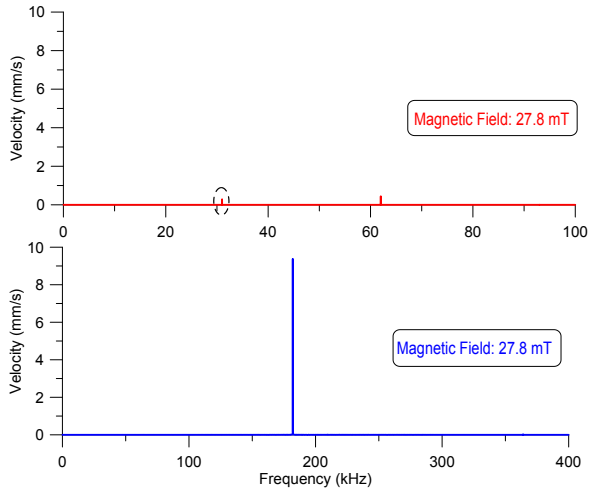

Figure 3.13: Compassion between the FFTs of the sensors response to an external magnetic field $B = 27.8$ mT in (a) forced-mode ($f_\circ = 31$ kHz) and (b) resonant-mode ($f_\circ = 182$ kHz) operation

the two sensor modes, Fig. 3.13, shows that the response increased 32-folds for the same external magnetic field when operated in resonant-mode.

The difference between forced-mode and resonant-mode operation is due to the dynamic amplification obtained by operating in the vicinity of the natural frequency. It is directly proportional to the quality factor of the sensor. Since the microplate has no release holes and experiments were conducted under atmospheric pressure, the squeeze film damping effect of the air cushion between the microplate and the bottom electrode resulted in significant damping. Comparing the undamped natural frequencies obtained using FEM to the damped natural frequencies obtained experimentally, we calculated the quality factor of the first out-of-plane bending mode as $Q = 1.47$ and of the first torsional mode as $Q = 1.27$. We conclude that the increased sensitivity and amplified response of resonant-mode operations realized above are quite modest. Further improvements to sensitivity and

response size can be obtained by operating the magnetic sensor in vacuum. Experience and literature suggests that soft vacuum should improve the quality factor by two orders-of-magnitude [68].

3.5 Sensor Calibration

3.5.1 Calibration using a Gaussmeter

To calibrate the sensor, we conducted an experiment to measure its response to variable magnetic strengths under identical operating conditions. The sensor chip was housed inside a specially designed test chamber that measures $(8.5 \times 5.5 \times 2.8)$ cm. Two permanent magnets were attached to the side walls of the test chamber parallel to each other, Fig. 3.14, such that a north and a south pole were facing each other. A breadboarded inside the test chamber was used to mount the sensor chip carrier. The excitation signals were delivered to the two bonding pads of the sensor through the breadboard and the chip carrier.

The velocity of the microplate response at point B was measured as the magnetic field strength was varied by adding pairs of identical magnets to the test chamber walls. In each case, the resulting magnetic field strength was measured using the sensor under test. A Gaussmeter, AlphaLab Inc. GM-2 [69], served as a truth measure and used to measure the magnetic field strength at the mid-point between the magnet stacks attached to opposite walls. During the experiment, the number of permanent magnet pairs placed inside the test chamber was increased from one to five pairs adding one pair at a time.

The sensor was operated in resonant mode. Throughout the experiment, the excitation signals were set to $V_{p1} = V_{p2} = 5$ V with a phase difference $\phi = 180^{\circ}$ and a common frequency of $f_{\circ} = 182$ kHz resulting in the passage of a current $I_c = 6.6$ mA in the current

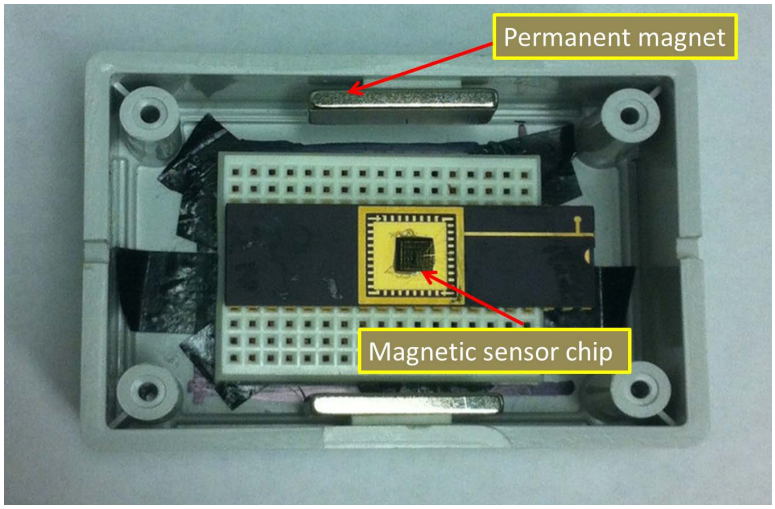

Figure 3.14: The magnetic sensor mounted inside the Gaussmeter test chamber

Table 3.5: The peak amplitude in the FFT of the measured velocity at the microplate edge as a function of the magnetic field strength B for a bias voltage of $V_{dc} = 0$ V.

# of magent pairs	B (mT)	$v(f_\circ)$ (mm/s)
1	29.90	15.260
2	30.91	16.696
3	31.75	17.476
4	32.42	18.878
5	33.25	20.238

loop. Tables 3.5 and 3.6 list the magnetic field strength measured using the Gaussmeter and the peak amplitude in the FFT of the measured velocity at the microplate edge (point B) as the number of magnet pairs increased from one to five for two test cases where the bias voltage was set to $V_{dc} = 0$ V and $V_{dc} = 2$ V.

The calibration curves of the sensor for both test cases are shown in Fig. 3.15. The sensor sensitivity, the slope of the magnetic field strength-microplate velocity curves, increased

Table 3.6: The peak amplitude in the FFT of the measured velocity at the microplate edge as a function of the magnetic field strength B for a bias voltage of $V_{dc} = 2$ V

# of magent pairs	$B(mT)$	$v(f_\circ)$ (mm/s)
1	29.9	31.486
2	30.9	33.959
3	31.7	37.924
4	32.4	40.454
5	33.2	46.306

from 1.48 (m/s)/T (blue line) at $V_{dc} = 0$ V to 2.9 (m/s)/T (red line) at $V_{dc} = 2$ V. The bias voltage creates an electrostatic field between the microplate and the bottom electrode and applies a static force bringing the microplate downward to an equilibrium point closer to the bottom electrode. The results show, increasing the bias voltage V_{dc} increases the sensor sensitivity and the absolute value of the measured microplate velocity.

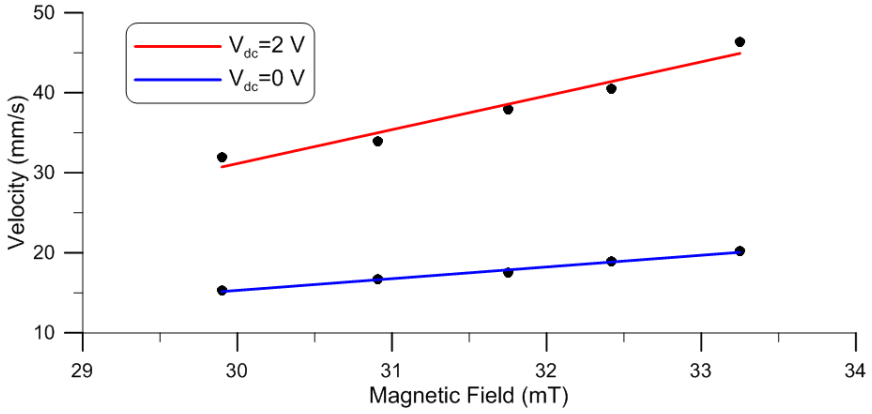

Figure 3.15: The calibration curves of the sensor for bias voltages of $V_{dc} = 0$ V (blue line) and $V_{dc} = 2$ V (red line)

3.5.2 Calibration using a Hall Effect sensor

The sensor chip was housed inside a specially designed test chamber that measures ($10.6 \times 6.3 \times 1.8$) cm^3. Two permanent magnets were attached to the side walls of the test chamber parallel to each other, Fig. 3.16, such that a north and a south pole were facing each other. A breadboarded inside the test chamber was used to mount the sensor chip carrier. The excitation signals were delivered to the two bonding pads of the sensor through the breadboard and the chip carrier.

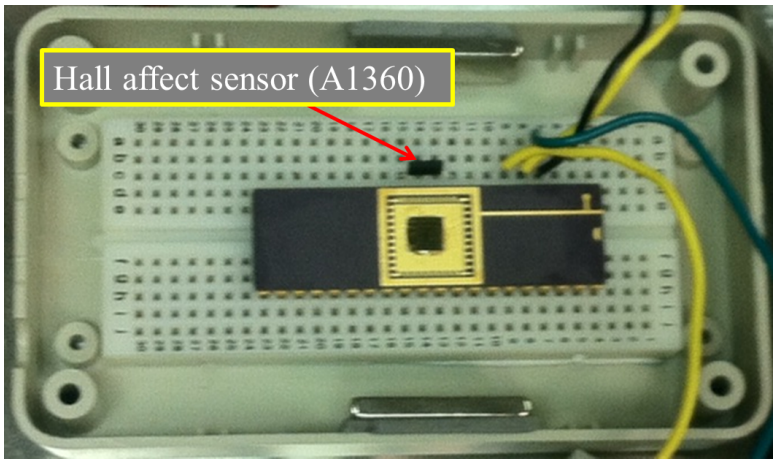

Figure 3.16: The magnetic sensor mounted inside the Hall effect test chamber

A Hall effect sensor, Allegro MicroSystems LLC A1360 [70], was placed beside the sensor chip carrier and served as a truth measure of the magnetic field strength between the magnet stacks attached to opposite walls shown in Fig. 3.16. During the experiment, the magnetic field strength, $B = 64$ mT, was fixed inside the test chamber. Using Hall effect sensor has an advantage that can introduced a fixed and accurate read out measurement compared to gauassmeter device.

Throughout the experiment, the excitation amplitude signals were set to $V_{p1} = V_{p2} =$

2.5 V with a phase difference $\phi = 180°$ and a common frequency of $f_\circ = 182$ kHz with zero DC bias, $V_{dc} = 0$ V, resulting in the passage of a current $I_c = 3.3$ mA in the current loop. A multi-scan points, Fig. 3.17(a), of the laser vibrometer for an 133 point area-grid over the microplate and a 42 point line-grid over each of the support beams were utilized to record displacement and velocity. The measured velocity and displacement at point A were averaged over microplate and with no DC voltage, $V_{dc} = 0$ V shown in Fig. 3.17(b).

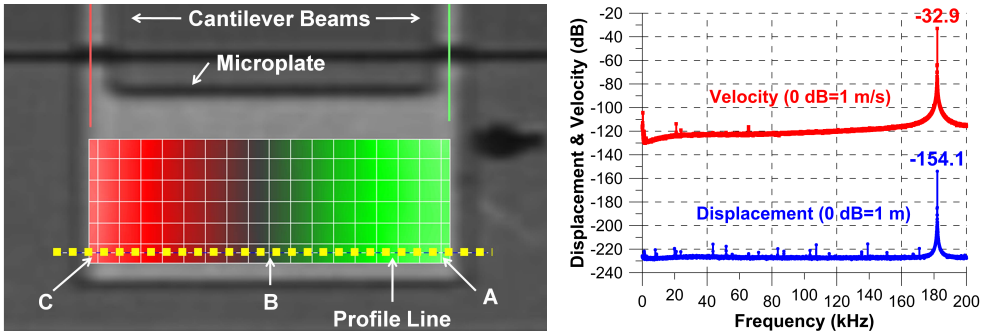

(a) (b)

Figure 3.17: (a) The area-grid and the line-grid $\overline{AC}$ used to measure the displacement and velocity of the microplate (b) Averaged frequency responses of the magnetic sensor excited by I_c= 3.3 mA sinusoidal current loop at 182 kHz with zero DC bias and external magnetic field of 64 mT

The configurations of the sensor at three phase angles within the torsional oscillations cycle are presented in Fig. 3.18(a). We measured displacement along line $\overline{AC}$, Fig. 3.17(a), on the microplate grid points, yellow line, at different phases, $\phi = 0°$, 90° and 270°. The microplate starts the cycle $\phi = 0°$ level with the measured displacement at point A close to zero (1.1 nm); after a quarter of a period $\phi = 90°$, one side of the microplate is displaced up while the other is displaced down with the displacement at point A reaching a cycle maximum (33 nm); and after another half cycle $\phi = 270°$ the two sides of the microplate

reverse direction with the displacement at point A reaching a cycle minimum (-33 nm). The minimal bias (displacement) along the microplate width at $\phi = 0°$, a node along the plate centerline and antisymmetric displacement profiles at quarter and three quarters of the period $\phi = 90°$ and 270°; all characteristics of a rigid body torsional mode of vibration.

The displacement and velocity of points A, B, and C in Fig. 3.17(a) are shown in Fig. 3.18(c) for a period of torsional oscillations. Comparing the velocity and displacement curves for all three points shows that the phase angles were identified correctly. The displacement measured along the centerline of the microplate, point B, is very close to zero throughout the cycle with a maximum measured displacement of ±80 pm, indicating minimal contributions of the bending mode to the overall microplate motion. The average signal-to-noise ratio (SNR) extracted from comparison of the displacement amplitude at points A and C to those at point B is SNR = 52.3 dB.

The static pull-in voltage of the sensor was measured experimentally as 6.9 V. We examined the sensor response in the operating range by measuring the frequency response of point A velocity at equally-spaced seven operating points $V_{dc} = 0, 1, 2, 3, 4, 5$, and 6 V at the same excitation torsional waveform $V_p = 2.5$ V and $\phi = 180°$. The sensor was placed in an external magnetic field of $B = 64$ mT. The frequency-response curves are presented in Fig. 3.19 for a frequency sweep in the range $f_\circ = [0, 200]$ kHz.

The response is dominated by the resonant motion in the vicinity of the torsional mode natural frequency $f_t = 182$ kHz. The response in the vicinity of the spurious bending mode natural frequency $f_b = 31$ kHz is not discernible (within the noise floor). All frequency-response curves are single valued and no evidence of nonlinearity, asymmetry, can be observed in those curves. Moreover, the measured peak response at resonance varies with the bias voltage indicating variation in the sensor response as the electrostatic field strength and gap distance vary.

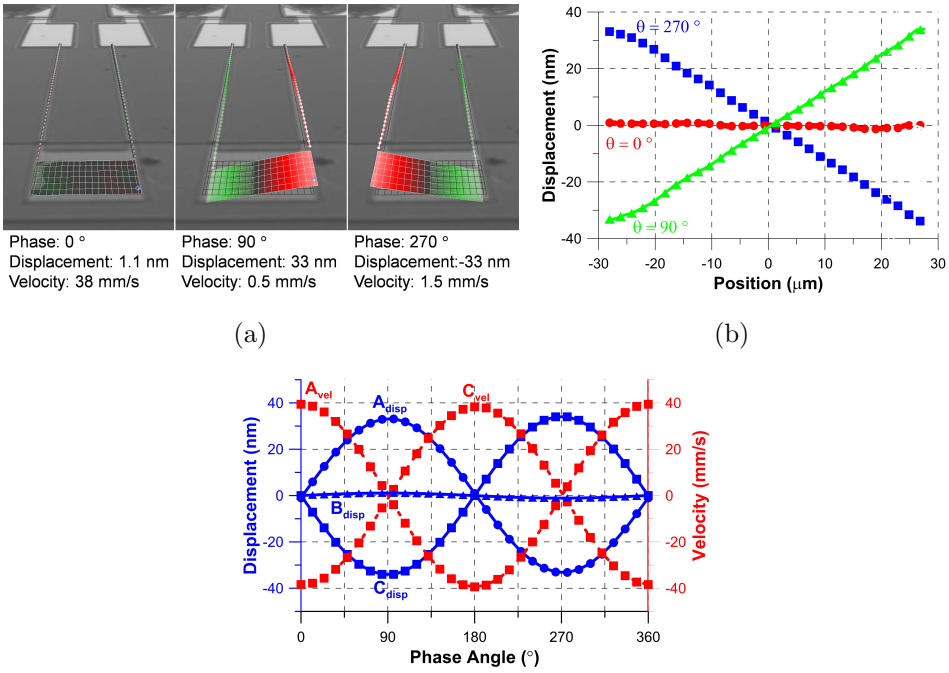

Figure 3.18: (a)The configuration of the sensor at phase angles $\phi = 0°, 90°$, and $270°$ within the torsional oscillations cycle.(b) The measured displacement of the grid point along line $\overline{AC}$ on the microplate at phase angles $\phi = 0°, 90°$, and $270°$ and (c) the measured displacement (blue solid lines) and velocity (red dashed lines) of points A, B, and C during a period of oscillations. Excitation current amplitude and frequency were set to $I_p = 3.3$ mA and $f_\circ = 182$ kHz and the external magnetic field to $B = 64$ mT

We generated the calibration curves of the magnetic sensor, Fig. 3.20, at seven operating points $V_{dc} = 0, 1, 2, 3, 4, 5$, and 6 V. The sensor was operated in resonant mode using the torsional waveform $V_p = 2.5$ V, $\phi = 180°$ and an excitation frequency of $f_\circ = 182$ kHz. Each calibration line represents a least-square linear fit of the measured velocity amplitude of point A as the external magnetic field strength is varied in the range of 56.8–79.8 mT.

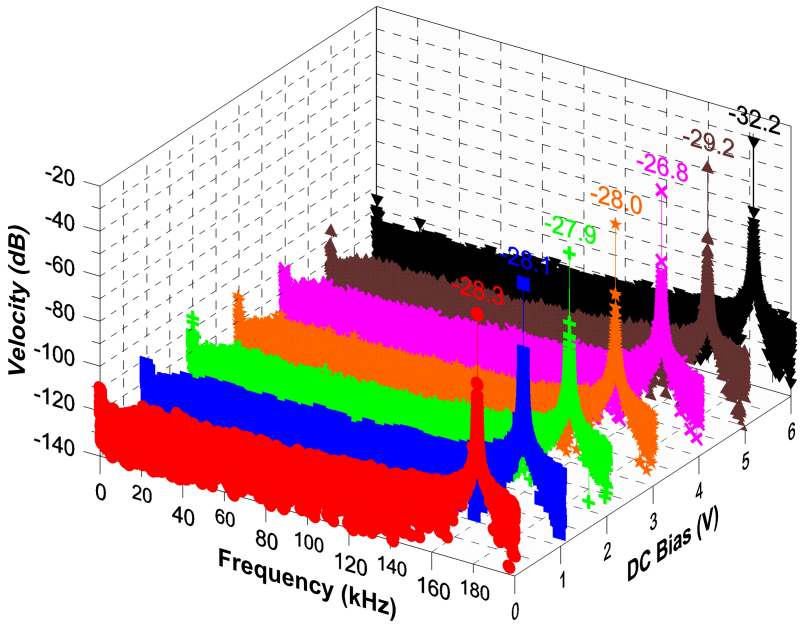

Figure 3.19: The frequency-response of point A velocity for a sensor bias voltage of $V_{dc} = 0, 1, 2, 3, 4, 5$, and 6 V, when excited by a current with amplitude and frequency of $I_p = 3.3$ mA and $f_\circ = 182$ kHz in a magnetic field of $B = 64$ mT (0 dB = 1 m/s)

For a given magnetic field strength, the absolute value of the measured velocity increases as bias voltage increases from 0 to 4 V, thereby decreasing the magnitude of the minimum measurable magnetic field. For voltages beyond that range, the absolute value of the measured velocity decreases as the voltage increases.

Table 3.7 lists the sensitivity and noise equivalent magnetic field strength, where the noise floor was set to 0.34 mm/s as reported above, section 3.4.2, for each operating point. Two domains can be identified in the sensor response. In the bias voltage range of 0–4 V, the sensitivity and noise equivalent field strength are relatively high and change slowly with bias voltage. On the other hand, in the bias voltage range 4–6 V, they drop precipitously as voltage increases. The difference in sensitivity and noise equivalent field strength between

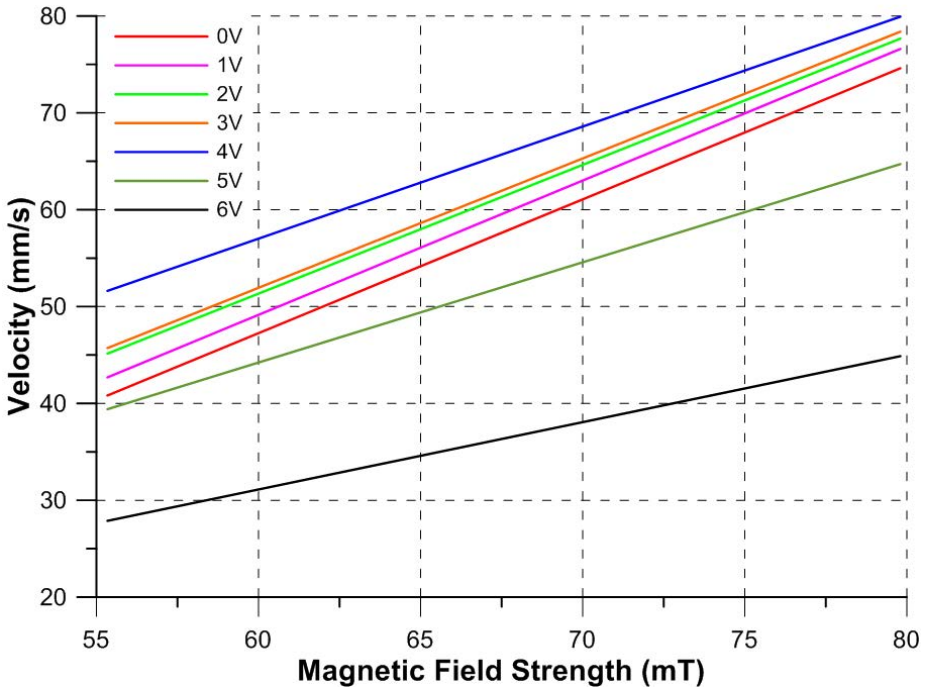

Figure 3.20: The calibration curves of the magnetic sensor for seven operating points at $V_{dc} = 0, 1, 2, 3, 4, 5$ and 6 V

the operating point at 1 V and 6 V is more than 100% demonstrating the sensor capability of on-the-fly sensitivity tuning by varying the bias voltage.

In the current sensor setup, variation in sensitivity among the different operating points is primarily due to elevated squeeze film damping levels experienced by the sensor as the microplate approaches the substrate under increased electrostatic forcing ($V_{dc} > 4$ V). In practical deployment where capacitance will be used to measure the sensor response, further sensitivity improvements will be derived from increased bias voltage and stronger electrostatic fields that will increase variation in capacitance for the same amount of displacement.

Table 3.7: Sensor sensitivity and noise equivalent field strength at seven operating points

Bias (V)	Sensitivity ((mm/s)/mT)	Noise equivalent field (mT)
0	0.866	26.0
1	0.870	24.8
2	0.834	21.6
3	0.838	21.4
4	0.728	11.0
5	0.649	17.5
6	0.436	15.7

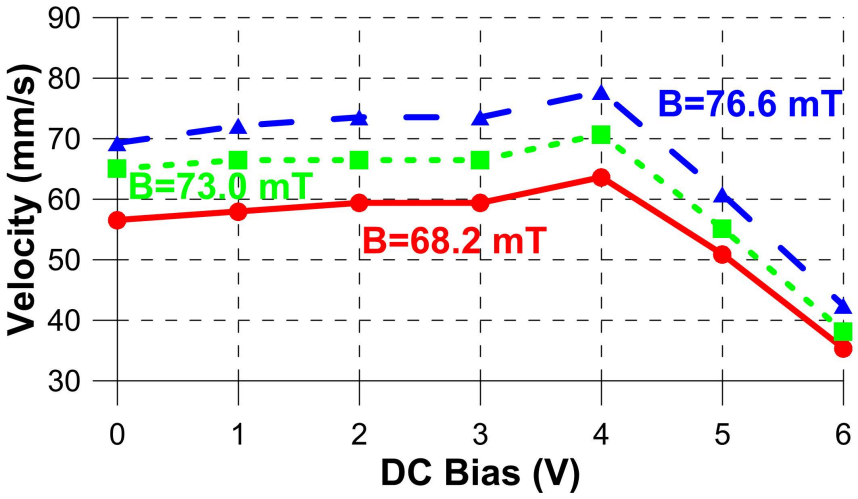

Figure 3.21: Measured velocity amplitude of point A as a function of bias V_{dc} for three levels of magnetic field strength

We conducted an experiment to delineate the operating range where the higher bias voltage increases sensitivity from the range where it decreases sensitivity. The torsional waveform $V_p = 2.5$ V and $\phi = 180$ ° was used to drive the magnetic sensor at its torsional resonant resonance ($f_\circ = 182$ kHz), while the bias voltage increased from 0 to 6 V at a

constant magnetic field B. The experiment was repeated for three levels of the external magnetic field $B = 68.2, 73.0$, and 76.6 mT.

Fig. 3.21 shows that the measured velocity increases consistently with increased magnetic field. It also shows that for a given magnetic field strength, the measured signal increases monotonically in the range $[0 - 4]$ V and decreases in the range $[4 - 6]$ V. This shows that the magnetic sensor operating point can be tuned within the former range to achieve higher sensitivity and latter range to achieve a larger dynamic range and a smaller noise equivalent field.

Chapter 4

Conclusions and Future Work

We developed and demonstrated to inertial MEMS sensors: an ethanol vapor sensor and an adjustable sensitivity magnetic field sensor.

4.1 Binary Gas Sensor

We utilized a novel sense mechanism that exploits the qualitative change in the sensor state before and after a static bifurcation in electrostatic MEMS, static pull-in, to implement a binary gas sensor. It indicates that the ambient ethanol concentration has exceeded a threshold amount by going into pull-in and sending a binary detection signal. Our implementation shows that this sense mechanism has the advantage of reducing requirements on readout electronics and enhancing robustness. Further, we showed that the sensitivity of bifurcation-based binary sensors represent the upper bound on the sensitivity of similar sized statically detected MEMS sensors.

The binary ethanol sensor was able to detect a concentration of 5 ppm in dry nitrogen at a set-off voltage of $\delta V = 1$ mV. We estimate the corresponding minimum detectable

mass is 165 pg. We also found that the sensitivity of P25DMA to ethanol vapor is one order-of-magnitude more than that of PANI doped with 10% NiO.

Our results show the viability and robustness of inertial MEMS sensors against external disturbances. This is particularly true for static-detection sensors designed to realize a low quality factor and, therefore, damp out those disturbances. Finally, we note that the binary sensor sensitivity depends on the voltage regulator resolution. Improving the operating voltage $V_\circ$ resolution can lower the set off voltage δV and further increase the sensor sensitivity.

4.2 Magnetic Field Sensor

We introduced a novel tunable MEMS magnetic sensor. It detects external magnetic fields by exploiting Lorentz force to excite a torsional vibration mode. We demonstrated that the coupling between electrostatic and electromagnetic actuation was minimal with a SNR = 52.3 dB and that the sensor response was linear for magnetic field strength up to $B = 79.8$ mT. We also demonstrated that the sensor sensitivity, minimum measurable field strength, and dynamic range can be tuned on-the-fly by varying the bias voltage. The sensor achieves better sensitivity and higher bandwidth when operated in resonant mode at $f_t = 182$ kHz. Finally, we identified two regions in the sensor parameter space; one region where the sensor sensitivity increased with bias voltage and another region where the higher bias voltage increased damping and reduced the sensor sensitivity.

4.3 Future Work

4.3.1 Dynamic Gas Sensor

The dynamic bifurcation-based sense mechanism should be explored. This mechanism exploits a dynamic bifurcation, a cyclic-fold bifurcation in this case, to implement binary dynamic gas sensors. A biased AC waveform will excite the sensor close to the cyclic-fold bifurcation and seek to use added mass to trigger the bifurcation, thereby maximizing sensitivity. A detector polymer will be deposited on the sense-plate to sorb ambient ethanol vapor. The frequency shift due to added mass will then trigger the sense-plate to go into pull-in due. The sensitivity of the dynamic gas sensor was predicted to be two orders-of-magnitude better than static bifurcation-based gas sensor [55].

4.3.2 Magnetic Field Sensor

The sensor was demonstrated in air to simplify the experimental procedure. Packaging the magnetic sensor in a vacuum will increase its sensitivity by several orders-of-magnitude and shrink the size of the undesirable operating region as the contribution of squeeze-film to overall damping is eliminated. Further, sensor deployment will require that it detects the displacement of the microplate by measuring capacitance variation in the microplate as it oscillates. This will add another layer of sensitivity improvement as higher bias voltage increases the strength of the electrostatic field and, therefore, the measured (output) signal.

References

[1] V. Kaajakari, *Practical MEMS*. Small Gear Publishing, 2009.

[2] N. Yazdi, F. Ayazi, and K. Najafi, "Micromachined inertial sensors," *Proceedings of the IEEE*, vol. 86, pp. 1640–1659, Aug 1998.

[3] PRIME Faraday Partnership, "An introduction to MEMS (Micro-electromechanical Systems)," 2002.

[4] K. Maenaka, "MEMS inertial sensors and their applications," in *5th International Conference on Networked Sensing Systems*, pp. 71–73, IEEE, June 2008.

[5] J. F. Rhoads, S. W. Shaw, and K. L. Turner, "Nonlinear dynamics and its applications in micro-and nanoresonators," *Journal of dynamic systems, Measurement, and Control*, vol. 132, no. 3, p. 034001, 2010.

[6] E. Robin, Laurent , Mounier, "Inertial sensor market moves to combo sensors and sensor hubs." 2013.

[7] G. A. Doty, D. Point, and G. Industries, "United States patent," 1987.

[8] B. Smith, "United States patent," 1995.

[9] X. Jianbing, S. Meng, and Y. Weizheng, "A high sensitivity micromachined accelerometer with an enhanced inertial mass SOI MEMS process," in *Nano/Micro Engineered and Molecular Systems (NEMS), 8th IEEE International Conference*, pp. 336–339, IEEE, 2013.

[10] P. Salvini, "Direct tuning of inertia sensors of a navigation system using the neural network approach," *Inverse Problems in Science and Engineering*, vol. 18, no. 1, pp. 131–144, 2010.

[11] Y. Chen, J. Jiao, B. Xiong, L. Che, X. Li, and Y. Wang, "A novel tuning fork gyroscope with high Q-factors working at atmospheric pressure," *Microsystem Technologies*, vol. 11, no. 2-3, pp. 111–116, 2005.

[12] G. A. Aydemir and A. Saranlı, "Characterization and calibration of MEMS inertial sensors for sate and parameter estimation applications," *Measurement*, vol. 45, no. 5, pp. 1210–1225, 2012.

[13] Z. Ding, Z. Luo, A. Causo, I. Chen, K. Yue, S. Yeo, and K. Ling, "Inertia sensor-based guidance system for upperlimb posture correction," *Medical engineering & physics*, vol. 35, no. 2, pp. 269–276, 2013.

[14] B. Ilic, Y. Yang, and H. Craighead, "Virus detection using nanoelectromechanical devices," *Applied Physics Letters*, vol. 85, no. 13, pp. 2604–2606, 2004.

[15] A. Zribi, A. Knobloch, W.-C. Tian, and S. Goodwin, "Micromachined resonant multiple gas sensor," *Sensors and Actuators A: Physical*, vol. 122, no. 1, pp. 31–38, 2005.

[16] K. Park, N. Kim, D. T. Morisette, N. Aluru, and R. Bashir, "Resonant MEMS mass sensors for measurement of microdroplet evaporation," *Microelectromechanical Systems*, vol. 21, no. 3, pp. 702–711, 2012.

[17] P. G. Datskos and I. Sauers, "Detection of 2-mercaptoethanol using gold-coated micromachined cantilevers," *Sensors and Actuators B: Chemical*, vol. 61, no. 1, pp. 75–82, 1999.

[18] S. Dohn, R. Sandberg, W. Svendsen, and A. Boisen, "Enhanced functionality of cantilever based mass sensors using higher modes and functionalized particles," in *Transducers, The 13th International Conference*, vol. 1, pp. 636–639, IEEE, 2005.

[19] N. Lobontiu, I. Lupea, R. Ilic, and H. G. Craighead, "Modeling, design, and characterization of multisegment cantilevers for resonant mass detection," *Journal of Applied Physics*, vol. 103, no. 6, p. 064306, 2008.

[20] H. Xie, J. Vitard, S. Haliyo, and S. Régnier, "Enhanced sensitivity of mass detection using the first torsional mode of microcantilevers," in *Mechatronics and Automation, International Conference*, pp. 39–44, IEEE, 2008.

[21] S. Dohn, O. Hansen, and A. Boisen, "Cantilever based mass sensor with hard contact readout," *Applied Physics Letters*, vol. 88, no. 26, p. 264104, 2006.

[22] H. Jensenius, J. Thaysen, A. A. Rasmussen, L. H. Veje, O. Hansen, and A. Boisen, "A microcantilever-based alcohol vapor sensor-application and response model," *Applied Physics Letters*, vol. 76, no. 18, pp. 2615–2617, 2000.

[23] W. Zhu, J. S. Park, J. L. Sessler, and A. Gaitas, "A colorimetric receptor combined with a microcantilever sensor for explosive vapor detection," *Applied Physics Letters*, vol. 98, no. 12, p. 123501, 2011.

[24] T. Thundat, P. Oden, and R. Warmack, "Microcantilever sensors," *Microscale Thermophysical Engineering*, vol. 1, no. 3, pp. 185–199, 1997.

[25] W. Zhang and K. L. Turner, "Application of parametric resonance amplification in a single-crystal silicon micro-oscillator based mass sensor," *Sensors and Actuators A: Physical*, vol. 122, no. 1, pp. 23–30, 2005.

[26] M. I. Younis and F. Alsaleem, "Exploration of new concepts for mass detection in electrostatically-actuated structures based on nonlinear phenomena," *Journal of Computational and Nonlinear Dynamics*, vol. 4, no. 2, p. 021010, 2009.

[27] P. S. Waggoner and H. G. Craighead, "Micro-and nanomechanical sensors for environmental, chemical, and biological detection," *Lab On a Chip*, vol. 7, no. 10, pp. 1238–1255, 2007.

[28] I. Dufour, E. Lemaire, B. Caillard, H. Debeda, C. Lucat, S. M. Heinrich, F. Josse, and O. Brand, "Effect of hydrodynamic force on microcantilever vibrations: applications to liquid-phase chemical sensing," *Sensors and Actuators B: Chemical*, vol. 192, pp. 664–672, 2014.

[29] I. Dufour, F. Josse, S. M. Heinrich, C. Lucat, C. Ayela, F. Ménil, and O. Brand, "Unconventional uses of microcantilevers as chemical sensors in gas and liquid media," *Sensors and Actuators B: Chemical*, vol. 170, pp. 115–121, 2012.

[30] M. E. Khater, E. M. Abdel-Rahman, and A. H. Nayfeh, "A Mass Sensing Technique For Electrostatically-Actuated MEMS," in *ASME 2009 International Design Engineering Technical Conferences and Computers and Information in Engineering Conference*, pp. 655–661, American Society of Mechanical Engineers, 2009.

[31] E. M. Abdel-Rahman, M. E. Khater, and A. H. Nayfeh, "Methods and systems for detection using threshold-type electrostatic sensors," June 1 2010. US Patent App. 12/791,293.

[32] W. Zhang, R. Baskaran, and K. L. Turner, "Effect of cubic nonlinearity on auto-parametrically amplified resonant MEMS mass sensor," *Sensors and Actuators A: Physical*, vol. 102, no. 1, pp. 139–150, 2002.

[33] Z. Yie, M. A. Zielke, C. B. Burgner, and K. L. Turner, "Comparison of parametric and linear mass detection in the presence of detection noise," *Journal of Micromechanics and Microengineering*, vol. 21, no. 2, p. 025027, 2011.

[34] V. Kumar, J. W. Boley, Y. Yang, H. Ekowaluyo, J. K. Miller, G. T.-C. Chiu, and J. F. Rhoads, "Modeling, analysis, and experimental validation of a bifurcation-based microsensor," in *ASME 2011 International Design Engineering Technical Conferences and Computers and Information in Engineering Conference*, pp. 177–186, American Society of Mechanical Engineers, 2011.

[35] R. Harne and K. Wang, "A bifurcation-based coupled linear-bistable system for microscale mass sensing," *Journal of Sound and Vibration*, vol. 333, no. 8, pp. 2241 – 2252, 2014.

[36] V. T. Rouf, M. Li, and D. A. Horsley, "Area-efficient three axis MEMS Lorentz force magnetometer," *IEEE Sensors Journal*, vol. 13, no. 11, pp. 4474–4481, 2013.

[37] J. G. Webster, *The measurement instrumentation and sensors handbook*. Electrical Engineering Handbook Series, Taylor & Francis, 1999.

[38] C. Chang, M. Tsai, Y. Liu, C. Sun, and W. Fang, "Development of multi-axes CMOS-MEMS resonant magnetic sensor using Lorentz and electromagnetic forces," in *MEMS2013*, pp. 193–196, 2013.

[39] S. M. Dominguez-Nicolas, R. Juarez-Aguirre, P. J. Garcia-Ramirez, and A. L. Herrera-May, "Signal conditioning system with a 4-20 mA output for a resonant magnetic field

sensor based on MEMS technology," *IEEE Sensors Journal*, vol. 12, no. 5, pp. 935–942, 2012.

[40] G. Langfelder and A. Tocchio, "On the operation of Lorentz-force MEMS magnetometers with a frequency offset between driving current and mechanical resonance," *IEEE Transactions on Magnetics*, vol. 50, no. 1, pp. 1–6, 2013.

[41] S.-W. Lai, T.-C. Kuo, and J.-F. Kiang, "CMOS-MEMS single-axis magnetic-field sensor for measuring geomagnetic field disturbance," in *International microsystems packaging assembly and circuits technology conference*, pp. 1–4, oct 2010.

[42] M. Li, V. T. Rouf, G. Jaramillo, and D. A. Horsley, "MEMS Lorentz force magnetic sensor based on a balanced torsional resonator," in *Transducers & Eurosensors XXVII*, pp. 66–69, 2013.

[43] E. Mehdizadeh, V. Kumar, and S. Pourkamali, "Sensitivity enhancement of Lorentz force MEMS resonant magnetometers via internal thermal-piezoresistive amplificationl," *IEEE Electron Device Letters*, vol. 35, no. 2, pp. 268–270, 2014.

[44] M. Thompson, M. Li, and D. Horsley, "Low power 3-axis Lorentz force navigation magnetometer," in *MEMS 2011*, pp. 593–596, Jan 2011.

[45] G. Langfelder, A. Tocchio, E. Lasalandra, and A. Longoni, "Comparison of Lorentz-force MEMS magnetometers based on different capacitive sensing topologies," in *Transducers & Eurosensors XXVII*, pp. 709–712, June 2013.

[46] A. Frangi, B. De Masi, G. Langfelder, and D. Paci, "Optimization of Lorentz-force MEMS magnetometers using rarefied-gas-theory," in *IEEE Sensors*, pp. 1–4, 2013.

[47] Z. Kádár, A. Bossche, P. Sarro, and J. Mollinger, "Magnetic-field measurements using an integrated resonant magnetic-field sensor," *Sensors and Actuators A: Physical*, vol. 70, no. 3, pp. 225–232, 1998.

[48] M. Stifter, F. Keplinger, H. Steiner, W. Hortschitz, and T. Sauter, "Principles of nonlinear MEMS-resonators regarding magnetic-field detection and the interaction with a capacitive read-out system," *Microsystem Technologies*, vol. 20, no. 4-5, pp. 783–791, 2014.

[49] M. Khater, *Use of instabilities in electrostatic Micro-Electro-Mechanical Systems for actuation and sensing*. PhD thesis, University of Waterloo, 2011.

[50] D. Koester, A. Cowen, R. Mahadevan, M. Stonefield, and B. Hardy, "PolyMUMPs design handbook," *MEMSCAP Inc*, 2003.

[51] K. Stewart, N. M. McManus, E. Abdel-Rahman, and A. Penlidis, "Doped polyaniline for the detection of formaldehyde," *Journal of Macromolecular Science, Part A*, vol. 49, no. 1, pp. 1–6, 2012.

[52] S. Senturia, *Microsystem design*. Springer US, 2013.

[53] M. E. Khater, M. Al-Ghamdi, S. Park, K. M. E. Stewart, E. M. Abdel-Rahman, A. Penlidis, A. H. Nayfeh, A. K. S. Abdel-Aziz, and M. Basha, "Binary MEMS gas sensors," *Journal of Micromechanics and Microengineering*, vol. 24, no. 6, p. 065007, 2014.

[54] A. H. Nayfeh, H. Ouakad, F. Najar, S. Choura, and E. Abdel-Rahman, "Nonlinear dynamics of a resonant gas sensor," *Nonlinear Dynamics*, vol. 59, no. 4, pp. 607–618, 2010.

[55] M. E. Khater, E. M. Abdel-Rahman, and A. H. Nayfeh, "A mass sensing technique for eletcrostatically-actuated MEMS," in *ASME 2009 International Design Engineering Technical Conferences and Computers and Information in Engineering Conference - IDETC/CIE*, pp. 655–661, American Society of Mechanical Engineers, 2009.

[56] A. H. Nayfeh and B. Balachandran, *Applied nonlinear dynamics*. John Wiley & Sons, 2008.

[57] V. Inc., "Wyko-NT1100 Optical Profiling System datasheet," www.veeco.com.

[58] P. Inc., "OFV-5000 Vibrometer Controller user manual," www.polytec.com.

[59] N. Wilson, "The risk of fire or explosion due to static charges on textile clothing," *Journal of Electrostatics*, vol. 4, no. 1, pp. 67 – 84, 1977.

[60] H. Kahn, A. Avishai, R. Ballarini, and A. Heuer, "Surface oxide effects on failure of polysilicon mems after cyclic and monotonic loading," *Scripta Materialia*, vol. 59, no. 9, pp. 912–915, 2008.

[61] H. Kahn, C. Deeb, I. Chasiotis, and A. H. Heuer, "Anodic oxidation during mems processing of silicon and polysilicon: Native oxides can be thicker than you think," *Microelectromechanical Systems, Journal of*, vol. 14, no. 5, pp. 914–923, 2005.

[62] C. Muhlstein, E. Stach, and R. Ritchie, "A reaction-layer mechanism for the delayed failure of micron-scale polycrystalline silicon structural films subjected to high-cycle fatigue loading," *Acta Materialia*, vol. 50, no. 14, pp. 3579–3595, 2002.

[63] J. Wibbeler, G. Pfeifer, and M. Hietschold, "Parasitic charging of dielectric surfaces in capacitive microelectromechanical systems (mems)," *Sensors and Actuators A: Physical*, vol. 71, no. 1, pp. 74–80, 1998.

[64] W. Merlijn van Spengen, "Mems reliability from a failure mechanisms perspective," *Microelectronics Reliability*, vol. 43, no. 7, pp. 1049–1060, 2003.

[65] A. T. Inc., "U1700 lcr meter," http://cp.literature.agilent.com/litweb/pdf/5990-3602ENDI.pdf.

[66] T. Li and T. Qin, *Physics and partial differential equations: Volume II*. Siam, 2014.

[67] S. Towfighian and M. Ozdogan, "Static modeling of a Bi-axial micro-mirror with sidewall electrodes.," in *ASME International Mechanical Engineering Congress and Exposition*, pp. 1–10, 2014.

[68] M. E. Khater, M. Akhtar, S. Park, S. Ozdemir, E. Abdel-Rahman, C. Vyasarayani, and M. Yavuz, "Contact Damping in MEMS Actuators," *APL Materials*, vol. Submitted, 2014.

[69] A. Inc., "DC Gaussmeter Model GM2," www.trifield.com/GM2/202012.pdf.

[70] A. M. LLC, "Hall effect sensor," www.allegromicro.com/datasheets/A1360-1-2-Datasheet.pdf.